Spatial characterization and simulation of new defects in corroded pipeline based on In-Line Inspections

Rafael Amaya-Gómez, Mauricio Sánchez-Silva, Felipe Muñoz, Franck Schoefs, Emilio Bastidas-Arteaga

Reliability Engineering and System Safety 241 (2024) 109697

Contents lists available at ScienceDirect

Reliability Engineering and System Safety

journal homepage: www.elsevier.com/locate/ress

Spatial characterization and simulation of new defects in corroded pipeline based on In-Line Inspections

Rafael Amaya-Gómez [a,c,*], Mauricio Sánchez-Silva [b], Felipe Muñoz [d], Franck Schoefs [c], Emilio Bastidas-Arteaga [e]

[a] Chemical Engineering Department, Universidad de los Andes, Cra 1E No. 19A-40, Bogotá, Colombia
[b] Department of Civil & Environmental Engineering, Universidad de los Andes, Cra 1E No. 19A-40, Bogotá, Colombia
[c] Université de Nantes, GeM, Institute for Research in Civil and Mechanical Engineering/Sea and Littoral Research Institute, CNRS UMR 6183/FR 3473, Nantes, France
[d] Process Safety Expert, Bogotá, Colombia
[e] Laboratory of Engineering Sciences for Environment, UMR CNRS 7356, La Rochelle University, France

ARTICLE INFO

Keywords:
Corroded pipeline
New defects
Complete Spatial Randomness
Interaction
Repulsion
Attraction

ABSTRACT

Onshore pipelines are exposed to corrosion degradation, facilitated by the pipeline's management and surrounding aggressive environmental conditions. Every 2 to 6 years, pipeline operators often conduct In-Line (ILI) inspections to screen for pipe damage using magnetic or ultrasonic sensors. Considering soil and fluid aggressive conditions, and the possibility of false alarms or a miss-detections from the inspection device, new defects, i.e., metal loss at either the inner or outer wall, should be expected to occur between consecutive inspections. Considering the possibility of "corrosion colonies" and their significance in the pipeline's reliability assessment, different authors have incorporated *new* corrosion defects in degradation and further reliability assessments using a Homogeneous Poisson Process. This process assumes that corrosion points are evenly distributed, which can be classified as conservative. This study aims to characterize the main spatial distribution of corrosion defects using the Complete Spatial Randomness (CSR) assumption under hypothesis testing. Additionally, it assesses how is the interaction between *new* and *old* defects from a repulsion–attraction perspective, and it proposes an alternative to simulate them for further reliability analyses. The suggested approach was applied in a real case study, obtaining that corrosion defects tend to be clustered and little repelled from those already detected.

1. Introduction

Corroded pipelines tend to degrade (i.e., metal loss) in a space-dependent manner either at the inner or outer wall. The different soil types around the pipeline, as well as the pipe's installation (underground vs. aboveground), use, and maintenance, all encourage this degradation. As an example, many studies have noted that soils with higher levels of chlorides, sulfates, and acidic pH, as well as the presence of bacteria, fungi, or algae, have a substantial impact on the pipe wall [1–3]. According to other findings, low flow rates (< 2 m/s) may result in competition between the corrosive species and the inhibitor, whereas high flow rates (> 6 m/s) may favor an erosion-corrosion in a H_2S/CO_2 medium with Sulfur deposition [4]. This space-dependent metal loss favors locations more prone to fail and where pipeline operators should pay more attention [5]. Considering a limit state perspective, this failure corresponds to an ultimate condition in which the resistance of the pipe cannot contain the fluid being transported, occurring in what is known as a Loss of Containment (LOC), leading to a leak, burst, or rupture of the pipeline [6]. Bearing in mind these fluids are commonly flammable, explosive, or even toxic, an uncontrolled release could trigger different accidental scenarios such as fires, explosions, or pollution scenarios [7]. Therefore, pipeline operators should support further interventions to avoid LOC events or expensive maintenance based on information from regular monitoring tools, such as In-Line (ILI) measurements [8,9].

In-Line inspection detects and measures corrosion defects along the pipeline, functioning as a screening tool for the pipeline condition at a given moment every 2 to 4 years. The outputs of this inspection include (Fig. 1): (i) The size of each corrosion defect in terms of their depth, length, and width detected by the inspection tool. For this purpose, the defect depth is greater than a predefined threshold, commonly taken as 10% of the pipe wall thickness. (ii) The location of

* Corresponding author at: Chemical Engineering Department, Universidad de los Andes, Cra 1E No. 19A-40, Bogotá, Colombia.
E-mail address: r.amaya29@uniandes.edu.co (R. Amaya-Gómez).

https://doi.org/10.1016/j.ress.2023.109697
Received 17 July 2022; Received in revised form 11 July 2023; Accepted 26 September 2023
Available online 29 September 2023

Nomenclature

α	Significance level
$\mathbb{E}[\cdot]$	Expected value function
$\mathbb{E}_r(n)$	Mean under the CSR assumption
ϵ_d	Defect depth measurement error
$\hat{\lambda_N}$	Estimated intensity of the new defects
$\hat{K}_r(r)$	Estimated Ripley's K-function
λ	HPP Poisson intensity
$\Lambda(x)$	Cox process
$\lambda(x)$	Inhomogeneous intensity
λ_N	Intensity of the new defects
$\mathcal{B}$	Subset of the evaluating window
$\mathcal{I}(\cdot)$	Indicator function
$\mathcal{K}(\cdot)$	Symmetric's kernel function
$\mathcal{N}$	Set of new points
$\mathcal{O}$	Set of old points
$\mathcal{P}$	Set of pattern points
$\mathcal{W}$	Rectangular window using the abscissa and the perimeter, i.e., $(\mathbb{A} \times \mathbb{P})$
$\mathcal{X}^2$	Pearson Chi-square test
$\measuredangle OPQ$	Angle formed by points O, P, and Q
$\mathbb{P}[\cdot]$	Probability measure
$\pi_1, \ldots, \pi_n$	Points permutations
$\sigma_r(n)$	Standard deviation under the CSR assumption
τ	Kendall's rank-correlation coefficient
$\tilde{\lambda}(u)$	Uncorrected kernel
$\tilde{\lambda}_D(u)$	Diggle's correction kernel
$\tilde{\lambda}_U(u)$	Uniform corrected kernel
$\tilde{\lambda}_{-i}$	Kernel-smoothing with the leave-one-out method
A	Study area
BG	Besag & Gleaves test
BR	Byth & Ripley test
CE_D	Clark & Evans test
$CvL(h)$	Cronie & Van Lieshout cross-validation estimate of the bandwidth
$d(i,j)$	Distance between the ith and jth points
d_{ILI}	Depth reported by the ILI tool
d_{ji}	jth Nearest neighbor of the ith event
$d_{ON}(i,j)$	Distance from the ith point of R_O to the jth point of R_N
d_{real}	Real corrosion depth
dy	Point-to-event nearest distance
dz	Nearest event neighbor under the T-square sampling
e_{ij}	Edge correction factor of the Ripley's K function
F-function	Cumulative frequency distribution of the spatial distance between a fixed point-to-nearest event
G-function	Cumulative frequency distribution of the nearest event-event
$H(r)$	Functional form (i.e., G, F, K, and L)
$H_{obs}(r)$	Observed functional
$H_{Theo}(r)$	Theoretical functional form
K, L-functions	Ripley's and its transformation. Mean number of points in concentric circles around each event
$K_{ON}(h)$	Cross-K function
$LCV(h)$	Loader likelihood cross-validation estimate of the bandwidth
m	Simulations in the Monte Carlo test
m_O, m_N	Old and New defects marks
n	Number of Points
$N(\mathcal{B})$	Number of points in $\mathcal{B}$
P_e	Perimeter
P_{attrac}	Attraction p-value
P_{repul}	Repulsion p-value
$q(\|\|x\|\|)$	Kernel smoothing border correction
R	Upper limit for the T_{MAX} and T_{DCLF} functions
r	Radius of concentric circles in K and L functions
R_O and R_N	Realizations of the old and new populations with n_O and n_N points
$s_1 \ldots, s_n$	Set of observations for the permutation test
t	Pipeline wall thickness
T_{DCLF}	DCLF test
T_{MAD}	MAD test
TH_N	Thompson test
X	Point process
API	American Petroleum Institute
CSR	Complete Spatial Randomness
DCLF	Diggle–Cressie–Loosmore–Ford test
HAZ	Heat-Affected Zone
HPP	Homogeneous Poisson Process
ICCP	Impressed Current Cathodic Protection
ILI	In-Line Inspection
IQR	Inter-quartile range
LOC	Loss of Containment
MAD	Maximum Deviation test
MFL	Magnetic Flux Leakage
MSE	Mean Square Error
MVPLN	Multivariate Poisson Lognormal Process
NHPP	Non Homogeneous Poisson Process
TTLQV	Two-termed Local Quadrat Variance
USDA	United States Department of Agriculture

each corrosion defect in terms of the pipe abscissa and its orientation using a clock-position analogy. (iii) The ILI results also include pipeline structural parameters (e.g., diameter, wall thickness), pipeline distribution (e.g., inclination, latitude/longitude, altitude), and operating parameters such as the maximum operating pressure [10].

New corrosion defects will appear between consecutive inspections. On the one hand, they can be related to the aggressiveness of the surrounding soil, fluid operation, and fluid properties. On the other hand, they can be missed during the first detection (i.e., miss-detection) or might raise a false alarm during the subsequent inspection. The latter case means that the inspection tool "detects" a shallow non-existing corrosion metal loss with a low probability of detection [10]. Without field measurements, it is impossible to determine why new defects appear, although there is unquestionably an "indication" of a new corrosion point [13]. Dealing with new defects from a reliability analysis implies two main processes of determining how many new defects would appear for a given period of time and where they will be spatially distributed. This information is critical to analyze possible "corrosion colonies", which make the pipeline more prone to fail [14], affecting further maintenance decisions.

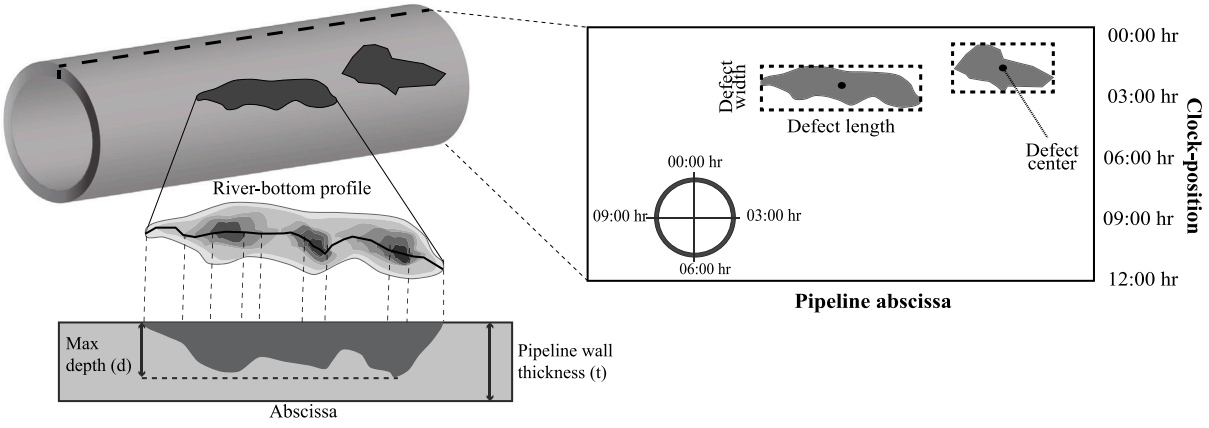

Fig. 1. Scheme of the dimensions of the corrosion defects.
Source: Modified from [11,12].

For this purpose, different approaches have been proposed to address new defects appearing between inspections. Some researchers have considered Poisson processes and Monte Carlo simulations to estimate the number of new defects and predict when they might occur [15,16]. These approaches typically consider a uniformly random location [16]. However, this assumption may be conservative given that corrosion clusters have been reported close welded joints [17], the circumferential location may be affected by coating disbondment [18], and that these clusters are likely to occur depending on their closeness [19]. Other alternatives include Multivariate Negative Binomial [20] or a Multivariate Poisson-Lognormal (MVPLN) [21,22] for evaluating defect count data. For instance, Wang et al. [22] considered an MVPLN model to predict the external corrosion of the pipe based on ILI data and soil corrosivity measurements. These authors also compared other count data approaches like the Multivariate Poisson model, Multivariate Negative Binomial model, and their univariate versions, considering the possibility of random or clustered patterns using a critical limit distance of 0.364 m. The MVPLN allows obtaining random variables that account for the spatial dependencies using the Markov Chain Monte Carlo (MCMC) algorithm from a Bayesian parameter inference, which can be used to assess the reliability of the pipeline but may omit the formation of future clusters.

Based on the mentioned above, some questions arise, such as: Are new corrosion defects, i.e., those being detected between inspections, randomly distributed along the pipeline? Is there any influence based on the surrounding soil, location of previous corrosion points, or pipe position? Do previous corrosion points tend to repel or attract new corrosion defects? Or are they spatially independent? If there is any spatial dependency, how new corrosion defects can be simulated to support further reliability assessments until a new ILI measurement is available?

This paper addresses these questions, seeking insights into how *new* corrosion points could be spatially distributed between consecutive inspections and how their spatial dependencies can be simulated. For this purpose, three main approaches are considered:

1. **How are *new* defects distributed?** A point pattern analysis is proposed based on the reported locations of each corrosion defect. This work evaluates the defects' distribution considering the Complete Spatial Randomness (CSR) assumption, which indicates that the points (i.e., corrosion defects) follow a uniform distribution across the evaluating window with a number of points coming from a Poisson distribution with a fixed intensity or that the points come from a Homogeneous Poisson Process. This approach is evaluated using hypothesis testing with clustered and dispersed point pattern alternatives. Different available tests use a nearest neighbor or functional perspectives, which were reviewed and selected for this purpose.
2. **How do *new* defects interact with *old* ones?** The location of the *new* defects could indicate an attraction or repulsion pattern, which in turn may favor a greater degree of a clustered or dispersed point pattern of the entire reported corrosion defects. As in the CSR assumption, this approach is evaluated using hypothesis testing with a null hypothesis of independence between the two sets of points used under Monte Carlo tests.
3. **How can *new* defects be simulated?** Predictions of the pipeline condition also require simulating new defects, which is why this work assesses a space-dependent point process to fit the *new* corrosion points, considering a Non-Homogeneous Kernel smoothing approach.

These three approaches contemplate a previous matching process between two consecutive inspections that allows discrimination of which defects were detected in the first inspection (i.e., *old* points) and which were not (i.e., *new* points). For this purpose, the methodology reported in Amaya-Gómez et al. [23] was used, based on the nearest neighbor perspective using Voronoi tessellation, a matching transformation, and correspondence and outliers' optimization approach.

The paper is structured as follows: Section 2 describes the Complete Spatial Randomness assumption and both possible alternatives: clustered and dispersed patterns. This section describes and selects the main methods for this analysis. Section 3 evaluates the repulsion/attraction test between the *new* and *old* defects. Section 4 describes the inhomogeneous point pattern analysis to simulate the distribution of the new defects. Section 5 describes spatial dependencies of the real case study, and the results and discussion are shown in Section 6. Finally, Section 7 presents some concluding remarks.

2. New defects distribution: are they randomly located?

Consider a set of n points ($\mathcal{P}$) on the pipeline either at the inner or outer wall, i.e., $\mathcal{P} = \{x_1, \ldots, x_n\}, x_i \in \mathcal{W} = (\mathbb{A} \times \mathbb{P})$, where $\mathcal{W}$ is the rectangular window formed by the pipeline abscissa ($\mathbb{A}$) and circumferential position ($\mathbb{P}$). Denote the number of points in a given area $\mathcal{B}$ as $N(\mathcal{B})$. This number of points is characterized to be finite for any subset area, i.e., $N(\mathcal{B}) < \infty, \forall \mathcal{B} \subset \mathcal{W}$. The Complete Spatial Randomness (CSR) states that $\mathcal{P}$ is uniformly distributed across the window with a number of points that follow a Poisson distribution with expected value λ, which is analogous that the $\mathcal{P}$ follow a homogeneous Poisson Process.

Formally, a point process X on $\mathcal{W}$ is a homogeneous Poisson point process with density λ if [24]:

(i) $\forall \mathcal{B} \subset \mathcal{W}$, $N(\mathcal{B})$ follow a Poisson distribution with mean $\lambda|\mathcal{B}|$, where $|\mathcal{B}|$ corresponds with the area of $\mathcal{B}$, and

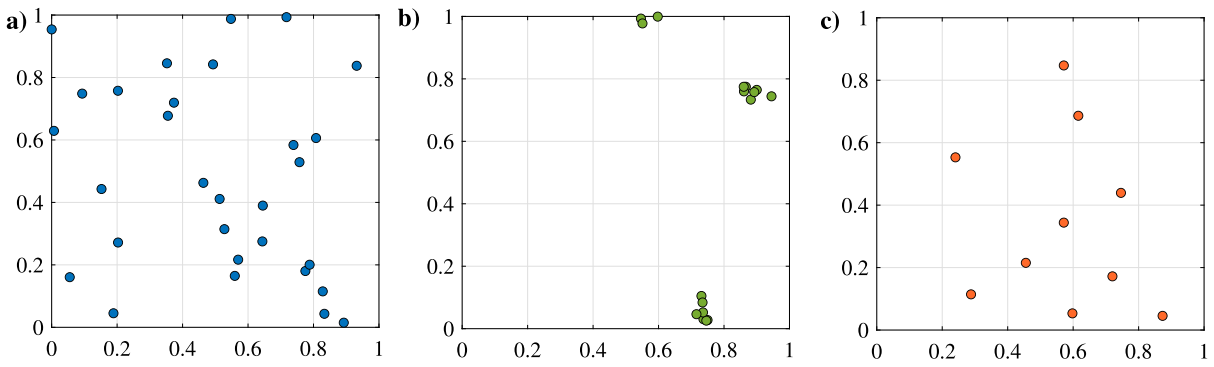

Fig. 2. (a) Random, (b) Cluster, and (c) Regular spatial dispersion points.

(ii) for any $n \in \mathbb{N}$ and $\mathcal{B} \subset \mathcal{W}$ with $0 < |\mathcal{B}| < \infty$, conditioned on $N(\mathcal{B}) = n$, then $X|_{\mathcal{B}}$ follow a Binomial point process with density $1/|\mathcal{B}|$.

Note that in case the intensity depends on the position (i.e., $\lambda(x)$), the process is known as inhomogeneous, and it follows that the expected number of points is determined by the area under this intensity function over the corresponding area, i.e., $\mathbb{E}[N(\mathcal{B})] = \mu(\mathcal{B}) = \int_{\mathcal{B}} \lambda(x)dx$. Besides, if X is invariant under translation, it is said stationary, and if invariant under rotation, it is known as isotropic.

The point distribution can be explained using a random realization of a Poisson (or Binomial) point process or as a result of spatial interactions regarding inhibitions or attractions among the points. Therefore, the patterns are usually classified considering random, cluster, or regular (inhibited) distributions; Fig. 2 illustrates these three spatial dispersion points considering stationary processes. The points in Fig. 2a are independent and randomly distributed, and they come from a realization of a Poisson Process with $\lambda = 50$. Fig. 2b shows an aggregated pattern where relevant spatial interactions can be perceived. This example comes from a Matern cluster process, which locates the parent points initially, and then offspring points are distributed uniformly around them using a given radius. This figure shows a realization of a Matern cluster process with 5 parent points and 10 "offspring" points at a distance lower than 0.05. Finally, Fig. 2c shows a more significant spatial inhibition than the CSR assumption, which comes from a sequential spatial inhibition process.

There are different approaches to evaluate the Complete Spatial Randomness assumption, given some points $\mathcal{P}$. In what follows, some of the most relevant approaches are described in detail below.

2.1. Quadrats and distance-based methods

Usually, quadrat counts and distance-based methods are commonly reported [25]. The quadrat method divides the study window into equally size quadrats – or non-overlapping areas – to later implement a Pearson $\mathcal{X}^2$ (Chi-square) test with the mean number of points per quadrat, following a Poisson distribution. Quadrats are one of the most recognized tests in the literature, considering continuous approaches such as the so-called TTLQV (Two-termed local quadrat variance). However, it is significantly sensitive to the window partition, so this work did not consider this test. Distance-based methods use either the nearest event-event separation (initial points $\mathcal{P}$) or the distance between random points with the events in $\mathcal{P}$.

This work considers the classical distance-based approaches of Clark & Evans (1954) with the Donnelly edge correction [26] and Thompson (1956) [27] due to their straightforward interpretation and prediction power [26,27]. Besides, the statistics of Byth & Ripley (1980) [28] and Besag & Gleaves (1973) [29] were selected following the recommendations of Dettloff [30], based on the power to identify non-randomness. The four distance-based methods are summarized in Table 1; they

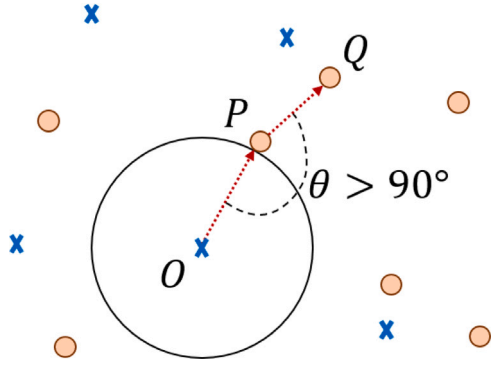

Fig. 3. T-square method description. The events are illustrated with circles and the crosses are the random points.

are denoted by CE_D, TH_N, BR, and BG, respectively; for further details, please refer to the corresponding reference or the reviews from Refs. [25,30].

The Clark & Evans aggregation ratio uses the mean distance of the nearest event-event with an expected distance following the CSR assumption. This ratio includes an edge correction associated with the bias produced by the events at the window's boundary, which would produce more considerable nearest-neighbor distances. The Thompson statistic is a generalization of Clark & Evans by implementing the second to the fifth nearest neighbors of each event. Byth & Ripley (1980) and Besag & Gleaves (1973) consider point-event distances where a random point O is initially added, and the distance to its nearest event P is determined. Finally, the distance from P to its nearest neighbor Q is measured. The approach of Besag & Gleaves is part of a particular class known as T-square, where the angle $\measuredangle OPQ = \theta > 90°$, as shown in Fig. 3.

2.2. Functionals and angle-based approaches

Other methods to evaluate the CSR assumption include approaches based on angles formed between the points and functionals [25]. For instance, the former case adds some random points and determines the angle formed between each of them and their two nearest events [31]. Despite some exciting capabilities for detecting non-randomness, its performance is usually less accurate than distance-based methods, particularly those with a T-square sampling [31]; therefore, they are also discarded. Functional approaches include the cumulative frequency distribution of the nearest event-event (G-function), the cumulative frequency distribution of the spatial distance between a fixed point-to-nearest event (F-function), and the mean number of points if circles with known radius are placed around each event (K and L-function).

Table 1
CSR tests for patterns with n points.

Statistic	Significance Test	Description	Ref.
$CE_D = \frac{\frac{1}{n}\sum_{i=1}^{n} d_{1i}}{\mathbb{E}_r}$	Z-test with $\mathbb{N}(\mathbb{E}_r, \sigma_r)$[a] $\mathbb{E}_r = 0.5\sqrt{\frac{A}{n}} + 0.0514\frac{P_e}{n} + 0.041\frac{P_e}{n^{3/2}}$; $\sigma_r = \frac{1}{n}\sqrt{0.07A + \left(0.037P_e\sqrt{\frac{A}{n}}\right)}$	Index of aggregation of the nearest neighbor with an edge correction.	[26]
$TH_N = \frac{\frac{1}{n}\sum_{i=1}^{n} d_{Ni}}{\mathbb{E}_r(n)}$	Z-test with $\mathbb{N}(\mathbb{E}_r(n), \sigma_r(n))$[a] $\mathbb{E}_r(n) = \sqrt{\frac{A}{n}}\left(\frac{(2n)!n}{(2^n n!)^2}\right)$; $\sigma_r(n) = \sqrt{\frac{A}{n}}\left(\sqrt{\frac{n}{\pi} - \mathbb{E}_r(n)^2}\right)$	Index of aggregation Nth nearest neighbors.	[27]
$BR = \frac{1}{n}\sum_{i=1}^{n} \frac{dy_{1i}^2}{dy_{1i}^2 + d_{1i}^2}$	Z-test with $\mathbb{N}\left(\frac{1}{2}, \frac{1}{12n}\right)$[b]	Ratio of the distance of random point-to-event and the events' nearest neighbors.	[28]
$BG = \frac{1}{n}\sum_{i=1}^{n} \frac{dy_{1i}^2}{dy_{1i}^2 + dz_{1i}^2/2}$	Z-test with $\mathbb{N}\left(\frac{1}{2}, \frac{1}{12n}\right)$[b]	Ratio of distances considering the T-square approach.	[29]

CE_D: Clark & Evans, TH_N: Thompson Nth nearest neighbor, BR: Byth & Ripley, and BG: Besag & Gleaves
A: Study area, P_e: perimeter, d_{ji}: jth nearest neighbor of the ith event, dy: point-to-event nearest distance, and dz: nearest event neighbor under the T-square sampling.

[a] If CE_D and TH_n <<1, the tests indicate a cluster point pattern; if CE_D and TH_n ≫1, a regular point pattern, and values near 1 accept the CSR assumption.

[b] If BR and BG ≫1/2, the tests indicate a cluster point pattern; if BR and BG <<1/2, a regular point pattern, and values near 1 accept the CSR assumption.

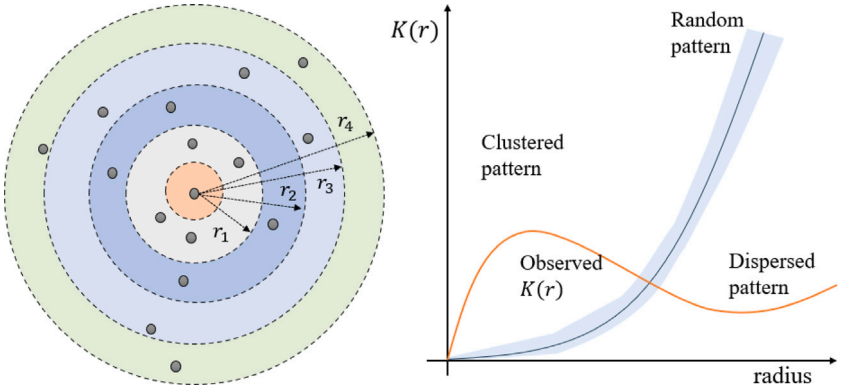

Fig. 4. Scheme of the Ripley's K-function.
Source: Adapted from Ref. [32].

These approaches compare the observed distributions with the empirical distribution under the CSR assumption, obtaining valuable information using confidence envelopes with Monte Carlo tests, see Fig. 4 for the case of the Ripley's K, where at the beginning is detected a clustered pattern, following for more dispersed data. From these approaches, the L-function (K-function transformation) was considered because of its recognized variance stabilization and natural interpretation, which is briefly described below.

The expected number of events within a distance r of a randomly chosen event can be estimated using Ripley's statistic as [33]:

$$\hat{K}_r(r) = \frac{A}{n(n-1)} \sum_i \sum_{j \neq i} e_{ij} \mathcal{I}(d(i,j) \leq r) \tag{1}$$

where A is the study area, $\mathcal{I}(\cdot)$ is the indicator function, $d(i,j)$ is the distance between the ith and jth points, and e_{ij} is an edge correction factor that deletes points if the circles around them are partially outside of the study window. Under CSR, it follows that $K_r(r) = \pi r^2$; if $K_r(r) > \pi r^2$, the point pattern is said to be clustered, whereas if the $K_r(r) < \pi r^2$ it follows a dispersed distribution. Therefore, the L-function has been proposed as follows [33]:

$$L(r) = \sqrt{\{K_r(r)/\pi\}} \tag{2}$$

This function states that a point pattern follows a CSR assumption similarly as in the K-function with $\mathbb{E}[L(r)] = r$. To evaluate this functional, different statistics have been considered using Monte Carlo tests, as discussed by Baddeley et al. [34] with the Maximum Deviation (MAD) and so-called Diggle–Cressie–Loosmore–Ford (DCLF) test. These tests can be applied for any functional mentioned before (i.e., K and L functions) by denoting them as $H(r)$ as follows:

$$T_{MAD} = \max_{0 \leq r \leq R} \left| H(r) - H_{Theo}(r) \right|, \quad T_{DCLF} = \int_0^R \left(H(r) - H_{Theo}(r) \right)^2 dr$$

where R is an upper limit about the interaction distance between points. $H_{Theo}(r)$ can be approximated as $\bar{H}(r) = \left(\frac{1}{m+1}\right)(H_1(r) + \cdots + H_m(r) + H_{obs}(r))$, being $H_i(r)$ for $i = 1, \ldots, m$ the simulated distance-based summary functions and H_{obs} the one obtained using the observation data [34]. In the case of Ripley's function $K_{Theo}(r) = \pi r^2$ and Besag's transformation $L_{Theo}(r) = r$. The null hypothesis of CSR is rejected if H_{obs} is higher than the kth largest simulated value with a significance level of $\alpha = k/(m+1)$ [34]. This Monte Carlo test was also applied for the distance-based methods considering a two-sided alternative. For this case, consider that j simulated values statistics are greater than the observed points, then the significance level can be calculated as $\alpha = 2\min(j+1, m+1-j)/(m+1)$ [34]. According to Baddeley et al. [34],

the main idea behind these Monte Carlo tests comes from the fact that if the null hypothesis of CSR is true, then the $m+1$ point patterns would be equivalent from a statistical point of view, i.e., they come from the same random distribution. The largest index's probability would then be $1/(m+1)$, which corresponds with the p-value.

3. Interaction of new defects: Repulsion or attraction?

After analyzing the hypothesis of CSR of *new* defects in Section 2, i.e., the possibility that corrosion points follow a random distribution, this section evaluates if *new* defects tend to be repelled or attracted by *old* corrosion points, or if they have no particular influence (i.e., random placements). This interaction may occur due to the cathodic protection mechanism or the corrosion cell. According to the U.S. Navy Department, some repulsion or attraction of positive metallic ions may occur depending on whether it is located at the node cathode or the anode. [35]. If more *new* points are close to *old* ones than expected under the independence assumption, there would be some "attraction" between the two populations. On the contrary, if there are significantly fewer *new* defects than expected, a "repulsion" between the two populations could be suggested. For ease of notation, let $\mathcal{O}$ be the set of *old* points and $\mathcal{N}$ as the set of *new* ones.

Different approaches have been proposed to evaluate the independent populations' assumption, including nearest-neighbor, Kendall's correlation rank, or cross-distance function tests. Nearest-neighbor tests generate random points and determine the distance to each population's nearest neighbors, denoted as d^1 and d^2, to estimate the distribution of both distances. Under the null hypothesis of independent populations, the distributions of d^1 and d^2 would also be independent [36]. Another approach was reported by Diggle & Cox [37], following a non-parametric test based on Kendall's rank-correlation coefficient τ. This approach simulates uniform random points and determines the distance to each population. However, in this case, the correlation is determined using signed indices from the distance difference of reference points. The estimated correlation discriminates against the cases of attraction (high positive values) and repulsion (high negative values) influences [37,38].

Finally, other approaches consider cell-count statistics based on cross versions of distance functions such as Ripley's K-function (see Eq. (1)), as in the case of Lotwick & Silverman [39] and Smith [38,40]. The approach of Lotwick & Silverman evaluates the influence of the two populations based on a cross-version of the distance K-function following a *random-shift* perspective. This perspective aims to evaluate different "samples" of both populations, as in CSR hypothesis testing with Monte Carlo tests. However, a test for the repulsion/attraction influence is more complicated than the CSR test because of the impossibility of replicating the particular spatial dependencies [40]. In this regard, they proposed shifting the evaluation window to simulate a new sample; they assumed a stationary process on the plane after wrapping the plane into a torus (i.e., donut) or replicating the entire window to form a "mosaic" [39]. Fig. 5 illustrates these random-shifting samples, considering two categories represented with white and blue points that are analogous to the *new* and *old* defects. Fig. 5a shows an initial point pattern with a random shifting, which is represented by an initial orange concentric circle that is shifted to the position of the red circle. This random shifting eventually would be complicated by those defects near the window's boundary, as they are subjected to an edge effect that hides the real interaction of both sets. Fig. 5b illustrates the same plane, but when the plane was wrapped into a torus. Finally, Fig. 5c duplicates this plane to address a continuous Mosaic shifting.

On the contrary, the approach of Smith contemplates the total number of observations n (i.e., n_1+n_2) and a null hypothesis in which populations are indistinguishable, so a permutation test considering a fixed number of points n is considered [38]. This work implements this alternative based on the comparison made by Smith with different point patterns [40]. Smith remarked that the *random-shift* approach of Lotwick & Silverman might hide global clustering in the mosaic (window replication) [38]. Also, Smith suggested that the approach of Diggle & Cox is limited for detecting small-scale relations between both populations, which is a general drawback for nearest-neighbor approaches that would only focus on local links. This approach will be explained in more detail in what follows.

Define a K cross-function K_{ON} that modifies the K-function for single populations (Eq. (1)). This function evaluates the expected number of points in the *new* dataset (i.e., $\mathcal{N}$) given a specific distance lag h from the set of *old* defects (i.e., $\mathcal{O}$). Let R_O and R_N be some realizations of these populations with a number of points of n_O and n_N in a given region S, respectively. The cross-K function is defined as follows [40]:

$$K_{ON}(h) = \frac{1}{\lambda_N}\mathbb{E}\left(\sum_{j=1}^{n_N}\mathcal{I}(d_{ON}(i,j)\le h)\right) \tag{3}$$

where $\mathcal{I}(\cdot)$ is an indicator function, $d_{ON}(i,j)$ is the distance from the ith point of R_O to the jth point of R_N, and λ_N is the intensity of the new defects. According to Smith [40], the number of points n_N and the distance between the two realizations $d_{ON}(i,j)$ would be considered random variables because the realizations have a different number of points that are randomly distributed based on the population intensities. The cross-K function can be obtained from the maximum likelihood estimate given below, where $\hat{\lambda}_N$ is the estimated intensity of $\mathcal{N}$ determined by the ratio between n_N and the area of the region S [40]:

$$\hat{K}_{ON}(h) = \frac{1}{\hat{\lambda}_N}\sum_{i=1}^{n_O}\sum_{j=1}^{n_N}\mathcal{I}(d_{ON}(i,j)\le h) \tag{4}$$

Given a set of observations $s_1,\dots,s_n$, the indistinguishable test of Smith establishes that every s_i could belong either to the $\mathcal{O}$ or $\mathcal{N}$ populations, i.e., the point mark $m_i = m_O$ or $m_i = m_N$. Consider the joint probability of the locations s_i and marks m_i of the observations $\mathbb{P}[(m_i)_i^n,(s_i)_i^n]$. Under the null hypothesis, the probability of having a given set of marks does not depend on the locations, and it is invariant under any permutation $\pi_1,\dots,\pi_n$ of the observed marks. Therefore, the sampling distribution under the null hypothesis, considering the observations with marks n_O and n_N, for n permutations, is given as follows [40]:

$$\mathbb{P}\left[(m_{\pi_1},\dots,m_{\pi_n})|(s_1,\dots,s_n),n_O,n_N\right] = \frac{1}{n!}$$

Based on the mentioned above, the *random-permutation* approach uses two point-patterns observations R_O and R_N for estimating the K cross-function $K_{ON}(h)$ for a given distance lag h. The observations are compared with M random permutations of these marks to estimate the attraction p-value as follows:

$$P_{attrac} = \frac{m^+ + 1}{M+1} \tag{5}$$

where m^+ is the number of permutations with a higher cross K function than in the initial observations. The repulsion p-value is determined as $P_{repul} = 1 - P_{attrac}$. This approach is repeated for a range of distance values $h_0 < h_1 < \cdots < h_p$.[1] In another paper, Smith [38] proposed a similar approach also including Kendall's correlation-rank coefficient τ, as in the case of Diggle & Cox [37], but it was not used in this work. For the corroded pipelines, every pipeline segment between joints was implemented as an independent sample following a similar procedure as in the function *k12_perm* of Smith [40].

[1] For a rectangular evaluation window with dimensions l_w and w_w, consider $h_p \le \min(l_w/2, w_w/2)$ to prevent edge effects.

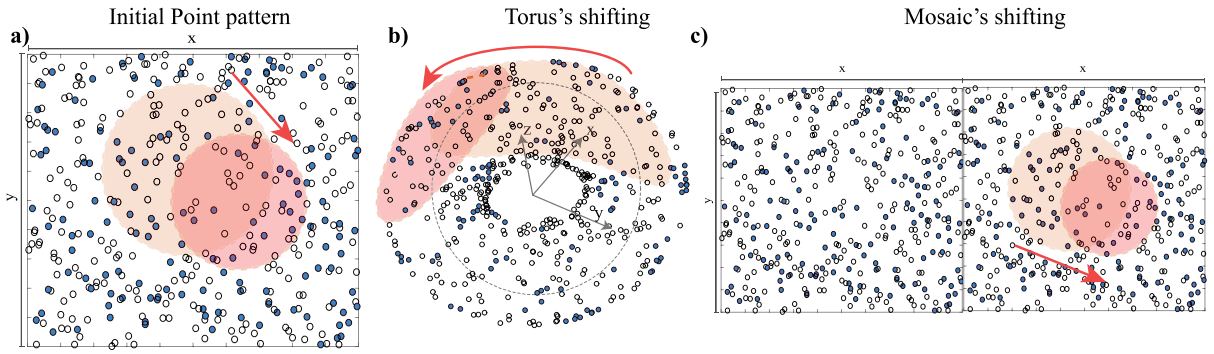

Fig. 5. Scheme of the random-shift K-function in the (a) initial point pattern, (b) torus wrap, and (c) mosaic wrap.

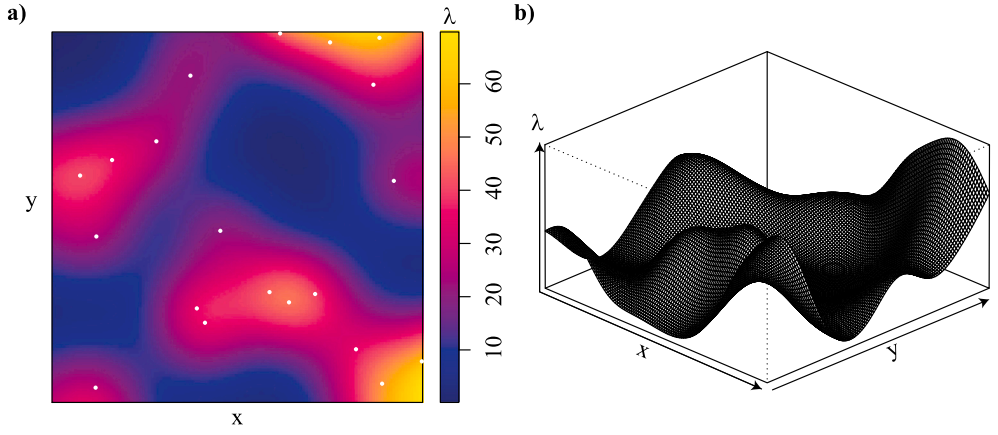

Fig. 6. Illustrative (a) kernel smoothing and (b) its surface perspective plot.

4. Point pattern analysis: where new defects could be located?

The rejection of the CSR assumption in a cluster or regular point patterns can be explained by *repulsion* or *attraction* forces produced by already detected defects, which means that defects may tend to inhibit new defects or rely close on them upon a given distance. The spatial distribution of defects could also follow an inhomogeneous Poisson process with a particular intensity function. This process would require estimating the intensity $\tilde{\lambda}(x)$ upon to a given location x, which can be determined using a kernel smoothing estimator as follows [41, §7.4.3]:

$$\tilde{\lambda}(x) = \frac{1}{h^2}\sum_{i=1}^{n} \mathcal{K}\left(\frac{\|x - x_i\|}{h}\right) / q(\|x\|), \tag{6}$$

where $q(\|x\|)$ is a border correction to deal with miss-observations close to the border of the evaluation area, h is a bandwidth associated with the smoothness level, and $\mathcal{K}(\cdot)$ is a symmetric's kernel function. Fig. 6a illustrates the result of the kernel smoothing of 20 random points in a square window, included as white points, and Fig. 6b depicts the surface perspective of the obtained intensity $\tilde{\lambda}$. The following sections will discuss the tuning of this intensity from the inspection data and the evaluation of interaction forces between new and old defects.

According to Baddeley et al. [42], the inhomogeneous intensity can be estimated based on three nonparametric approaches, namely, an uncorrected kernel $\tilde{\lambda}(u)$, a uniform corrected kernel $\tilde{\lambda}_U(u)$, or an approach using the Diggle's correction $\tilde{\lambda}_D(u)$. These estimators are given as follows:

$$\tilde{\lambda}(u) = \sum_{i=1}^{n} \mathcal{K}(u - x_i) \tag{7}$$

$$\tilde{\lambda}_U(u) = \frac{1}{e(u)}\sum_{i=1}^{n} \mathcal{K}(u - x_i) \tag{8}$$

Table 2
Common used Kernels.
Source: Adapted from [43].

Kernel	Equation
Uniform	$\mathcal{K}(u) = \frac{1}{2}$
Epanechnikov	$\mathcal{K}(u) = \frac{3}{4}\left(1 - u^2\right)$
Biweight (Quartic)	$\mathcal{K}(u) = \frac{15}{16}\left(1 - u^2\right)^2$
Triweight	$\mathcal{K}(u) = \frac{35}{32}\left(1 - u^2\right)^3$
Gaussian	$\mathcal{K}(u) = \frac{1}{\sqrt{2\pi}}\exp\left(-\frac{u^2}{2}\right)$

Support of all kernels is $|u| \leq 1$, except for the Gaussian with $\mathbb{R}$.

$$\tilde{\lambda}_D(u) = \sum_{i=1}^{n} \frac{1}{e(x_i)}\mathcal{K}(u - x_i) \tag{9}$$

where $\mathcal{K}(u)$ is a kernel function representing a probabilistic density with support given by the window $\mathcal{W}$, i.e., outside this window, is zero. This kernel is commonly assumed to follow an isotropic Gaussian probability density, but other possibilities are also contemplated (see Table 2). $e(u)$ is a correction for the bias produced from the edge effect given as follows [42]:

$$e(u) = \int_{\mathcal{W}} \mathcal{K}(u - v)dv$$

These kernel estimators have some particularities, as remarked by Baddeley et al. [42]. For instance, the uncorrected approach $\tilde{\lambda}(u)$ omits the edge effect, affecting the intensity around the window's boundary. Over-smoothing with low-intensity values would be expected in this case, which may trigger a strong negative bias. The three approaches are controlled by a bandwidth parameter that smooths the intensity

associated with the standard deviation of the predicted kernel. This parameter is more relevant for the intensity prediction, even for the kernel type [41]. The choice follows a trade-off between the kernel bias and its variance. According to Baddeley et al. [42], higher bandwidth parameters would contribute to a higher bias (over-smoothing) and a lower variance. There are different approaches to estimating this bandwidth. Some of them include the algorithm proposed by Diggle [44] based on the mean square error, the likelihood cross-validation method proposed by Loader [45], and the non-parametric approach of Cronie & Van Lieshout [46]. They are briefly explained below.

The Cross-validated selection method of Diggle assumes that the intensity $\lambda(x)$ comes from a Cox Process $\Lambda(x)$. Denote as $N(x,h)$ the number of points of $\Lambda(x)$ in a distance h (centered at x), then the intensity can be estimated by $\tilde{\lambda}(x) = N(x,h)/(\pi h^2)$. The approach of Diggle considers a Cross-Validation approach minimizing the Mean Square Error shown below, considering the expectation from the distribution of the Cox Process [47].

$$MSE(h) = \mathbb{E}\left[\{\tilde{\lambda}(x) - \Lambda(x)\}^2\right]$$

The approach of Loader [45] considers a maximum likelihood Cross-validation approach to select the bandwidth's h. It assumes that the intensity comes from an inhomogeneous Poisson Process. The likelihood estimate is given by:

$$LCV(h) = \sum_{i=1}^{n} \log(\tilde{\lambda}_{-i}(x_i)) - n\left(\int_{\mathcal{X}} \tilde{\lambda}(u)du - 1\right)$$

where $\tilde{\lambda}_{-i}$ is the kernel-smoothing with the leave-one-out method; that is, it is determined with the bandwidth h without the ith point. $\tilde{\lambda}(u)$ is the kernel-smoothing, also with this bandwidth, at location u, and $\mathcal{X}$ is the support of the point process.

The method of Cronie & Van Lieshout [46] selects the bandwidth that minimizes the discrepancy of the area of the window observation $\ell(W)$ and reciprocal estimates of the density (at the points of the process), as follows:

$$CvL(h) = \left(\ell(W) - \sum_{i=1}^{n} \frac{1}{\tilde{\lambda}(x_i)}\right)^2$$

Besides these approaches, other authors have proposed different thumb rules like those reported by Silverman or Scott [48]. These rules of thumb estimate the bandwidth as $h = Cn^{-1/5}$, where $C = 0.9\min(s, IQR/1.34)$ and $C = 1.06\min(s, IQR/1.34)$ for the Silverman and Scott criteria, respectively. In these expressions, s is the standard deviation of the sample, IQR is the interquartile distance, and n is the number of sample points. These last approaches assume that the kernel and the bandwidth do not change in the evaluating window, but the intensity may depend greatly on the position.

5. Case study description

5.1. Main parameters

The case study concerns an API 5LX52 pipeline 45 km long, its height lies between 2560 to 2660 m above sea level, and it has six main valves. The pipeline has welded covers, supports, and flanges along the route. The pipeline is mainly localized in plain terrain with inclinations lower than 7°; it crosses two mountains and two urban zones. The mean length for the pipe joints is 10.7 m, and the welded cover is 0.7 m. Near kilometer 33, there is a river crossing, whereas the last 10 km are close to urban zones. Regarding the pipeline operation, it was reported a mean operating velocity of around 2.2 m/s and an operating temperature from 27 to 34 °C. Please refer to Amaya-Gómez et al. [49] for further details.

The pipeline has a nominal wall thickness of 6.35 mm and an external diameter of 273.1 mm. The analysis presented here was based on data obtained from two consecutive ILI measurements two years apart. The inspection measurements corresponded with two spreadsheets that include the pipe tally, list of defects, and list of clusters, as described by the Pipeline Operator Forum [10], covering 23.708 (2.862) corrosion defects for the inner (outer) wall for the first inspection, and 43.399 (4.264) defects for the inner (outer) wall at the second inspection. According to the ILI report, this diameter is maintained along the entire abscissa, while the wall thickness exhibits greater variability due to welded covers, valves, dents, and manufacturing flaws. The defects measuring tool was a Magnetic Flux Leakage (MFL). Based on information reported in Amaya-Gómez et al. [14] about the inspection vendor, it can be assumed a circumferential uncertainty of 5° during the inspection. The measurement uncertainties of the defect depth, length, and width are given by $d_{ILI} = d_{real} \pm \epsilon_d$, $l_{ILI} = l_{real} \pm \epsilon_l$, and $w_{ILI} = w_{real} \pm \epsilon_w$, where $d_{ILI}, l_{ILI}, w_{ILI}$ stand for the depth, length, and width reported by the ILI tool, and $\epsilon_d, \epsilon_l, \epsilon_w$ are their measurement errors, respectively. The measurement errors can be assumed to follow normal distributions centered at 0 with standard deviations obtained from information provided by inspection vendors [50]. It is reasonable to assume that $\epsilon_d = 0.1t$ with t the nominal wall thickness, $\epsilon_l = \epsilon_w = 11.70$ mm, considering a length and width accuracy of 15 mm with the confidence of 80% of the data. Further details of the case study cannot be provided for confidential agreements.

Table 3 shows a broad classification of the soil along the pipeline following the taxonomy of the USDA (United States Department of Agriculture). The pipeline has a bituminous coating of coal tar and an impressed current cathodic protection (ICCP) system. Coal tar is composed principally of aromatic hydrocarbons that constitute the foremost liquid condensate of the distillation process from coal to coke [51]. Coal-tar-based coatings have exceptional moisture resistance; however, some disadvantages are poor light stability and possible cracks at the upper surface from an oxidation process due to a higher level of unsaturation [51]. Thicker layers can protect the pipeline, but delamination is expected more than a polyethylene coat [52].

5.2. Main descriptors of corrosion defects

Most defects are concentrated on the inner wall, which is somehow expected due to the coal-tar coating that protects the outer wall; a summary of statistics of these datasets is depicted in Table 4. Because further information about defects' shape is not available in ILI, the maximum rather than the average depth for each defect will be considered for being more conservative with the metal loss (Fig. 1).

Following the matching approach proposed by Amaya-Gómez et al. [23] based on a Voronoi nearest mixed criterion, it was classified each metal loss from the last inspection as *old* – i.e., matched – and *new* – i.e., not matched defects. Table 5 shows the summary of the corrosion extent from both sets. Note that larger and wider defects appeared in the *new* dataset but with shallow depths, associated with uniform corrosion that may not have initially been detected in the first inspection.

6. Results and discussion

In this section, key findings from three major analyses are presented: (i) the CSR hypothesis testing that determines whether corrosion defects are randomly distributed depending on the inner or outer side of the pipeline and the type of soil surrounding it; (ii) the repulsion-attraction test to determine whether *new* defects interact with *old* ones, and (iii) kernel smoothing estimator method that simulates the spatial distribution of the *new* defects.

6.1. Complete spatial randomness (CSR) assumption evaluation for new defects

As explained in Section 2, six independent tests were considered for this objective. These tests were on their predictive ability using $m = 99$

Table 3
Pipeline segmentation based on the USDA soil classification.

Segment[a]	Category	Classification	ID
0.00–6.66 km	Complex	Pachic Melanudands (50%), Andic Dystrudepts (20%), Aeric Endoaquepts (15%), Aquic Hapludands (15%)	Soil 1
6.66–8.2 km	Association	Humic Lithic Eutrudepts (35%), Typic Placudands (25%), Dystric Eutrudepts (25%)	Soil 2
8.2–9.66 km	Complex	Pachic Melanudands (50%), Andic Dystrudepts (20%), Aeric Endoaquepts (15%), Aquic Hapludands (15%)	Soil 1
9.66–11.61 km	Association	Humic Dystrudepts (60%), Typic Hapludalfs (40%)	Soil 3
11.61–13.48 km	Complex	Pachic Haplustands (35%), Humic Haplustands (35%), Fluventic Dystrustepts (30%)	Soil 4
13.48–14.86 km	Association	Aeric Epiaquents (60%), Fluvaquentic Endoaquepts (40%)	Soil 5
14.86–15.89 km	Complex	Humic Dystrustepts (40%), Typic Haplustalfs (35%), Fluvaquentic Endoaquepts (25%)	Soil 6
15.89–17.62 km	Association	Aeric Epiaquents (60%), Fluvaquentic Endoaquepts (40%)	Soil 5
17.62–18.65 km	Complex	Humic Dystrustepts (40%), Typic Haplustalfs (35%), Fluvaquentic Endoaquepts (25%)	Soil 6
18.65–18.84 km	Association	Typic Endoaquepts (40%), Aeric Endoaquepts (30%), Thaptic Hapludands (20%)	Soil 7
18.84–21.40 km	Complex	Humic Dystrustepts (40%), Typic Haplustalfs (35%), Fluvaquentic Endoaquepts (25%)	Soil 6
21.40–22.63 km	Association	Typic Endoaquepts (40%), Aeric Endoaquepts (30%), Thaptic Hapludands (20%)	Soil 7
26.07–27.35 km	Complex	Pachic Haplustands (35%), Humic Haplustands (35%), Fluventic Dystrustepts (30%)	Soil 4
27.35–28.22 km	Urban zone	–	–
28.22–30.52 km	Association	Aeric Epiaquents (60%), Fluvaquentic Endoaquepts (40%)	Soil 5
30.52–33.10 km	Complex	Pachic Haplustands (35%), Humic Haplustands (35%), Fluventic Dystrustepts (30%)	Soil 4
33.10–35.45 km	Association	Typic Endoaquepts (40%), Aeric Endoaquepts (30%), Thaptic Hapludands (20%)	Soil 7
35.45–45.00 km	Urban zone	–	–

[a] Both ILI did not include information of the segment from 22.63 to 26.07 km.

Table 4
Summary of corrosion defects along the abscissa.

Parameter	Mean (Coefficient of Variation)			
	ILI-1 Inner wall	ILI-2 Inner wall	ILI-1 Outer wall	ILI-2 Outer wall
Average depth (%t)	5.49 (0.26)	5.29 (0.27)	7.28 (0.49)	6.77 (0.46)
Maximum depth (%t)	11.54 (0.21)	11.14 (0.19)	15.84 (0.46)	14.62 (0.43)
Length (mm)	26.07 (0.49)	26.07 (0.43)	28.07 (0.48)	27.37 (0.44)
Width (mm)	22.5 (0.40)	25.92 (0.53)	28.81 (0.67)	32.60 (0.75)
Number of defects	23708	43399	2862	4264

Table 5
Summary corrosion extent of the *new* and *old* sets [23].

Set	Parameter	Inner wall						Outer wall					
		Min	Q_1	Q_2	Mean	Q_3	Max	Min	Q_1	Q_2	Mean	Q_3	Max
old	Depth	10	10	11	11.64	12	36	10	11	14	16.8	20	70
	Length	10	18	22	25.31	30	85	10	19	24	27.47	33	109
	Width	14	18	20	26.82	30	255	16	19	28	35.69	41	270
new	Depth	10	10	10	10.89	11	36	10	10	11	13.11	14	36
	Length	10	18	23	26.44	32	92	10	19	25	27.3	33	132
	Width	12	18	20	25.47	28	271	16	18	24	30.52	35	813

*Q_1, Q_2, and Q_3 are the first, second and third quartiles of the data, respectively.

random simulations in the Monte Carlo tests to ensure a minimum *p*-value of 0.01, following the indications of Baddeley et al. [34]. The tests consider aggregation indexes from the nearest neighbor (Clark & Evans and Thompson tests), the ratio of a random point-to-event distance (Byth & Ripley test), the ratio of distances using the T-square approach (Besag & Gleaves), and two functional approximations from Ripley's transformation *L* (DCLF and MAD tests). The sample criterion suggested by Dettloff [30] was applied in all cases. According to this standard, a sampling proportion between 10% to 50% would increase the probability of a possible violation of independence with reflexive neighbors. In the present study, a sampling of 50% was considered. The results are divided into three main analyses: (i) the entire soil segments, (ii) the mean ratio per segment (between consecutive joint welds), but excluding 1 m to the welds, and (iii) the welds up to 1 m for each side, as illustrated in Fig. 7.

6.1.1. Results for CSR tests applied to the new defects

The *p*-values obtained for each test and soil section in the inner wall are shown in Table 6. For the analysis, only segments with more than 20 points were included to prevent any significant bias from segments with few corrosion points. This table classifies the results into clustered (Green cells) or Random (Yellow cells), with a significance level of 5%. The random results occurred when the CSR test failed using both the clustered and dispersed alternatives. In terms of findings, all tests rejected the CSR hypothesis favoring a clustered point pattern, with the exception of the approach proposed by Besag & Gleaves, which failed to reject this assumption. The generated *p*-values for this test were close to the specified significance threshold. This result could imply that the Besag & Gleaves test may not be appropriate to evaluate the pipeline CSR assumption. Note that this test relates to the specific class of T-square distance, which applies the nearest distance between two events with an angle larger than 90° and the closest distance between random events to an existing event (Fig. 3). In this work, the unwrapped plane was used as the analysis's window, which might result in some additional edge problems for this specific test.

Concerning the results of the outer wall, Table 7 also shows a prevalent cluster pattern, except from the test of Besag & Gleaves and few segments for the Clark & Evans method. For segments with a low number of defects, higher *p*-values for the Clark & Evans test were achieved. Such segments could be affected by the sampling technique that attempted to avoid reflexive nearest neighbors. It should be noted that Thompson's method essentially employs the same idea but applies it to the second nearest neighbor. This method identified a clustered pattern for each segment; hence, this result may not be definitive. Also,

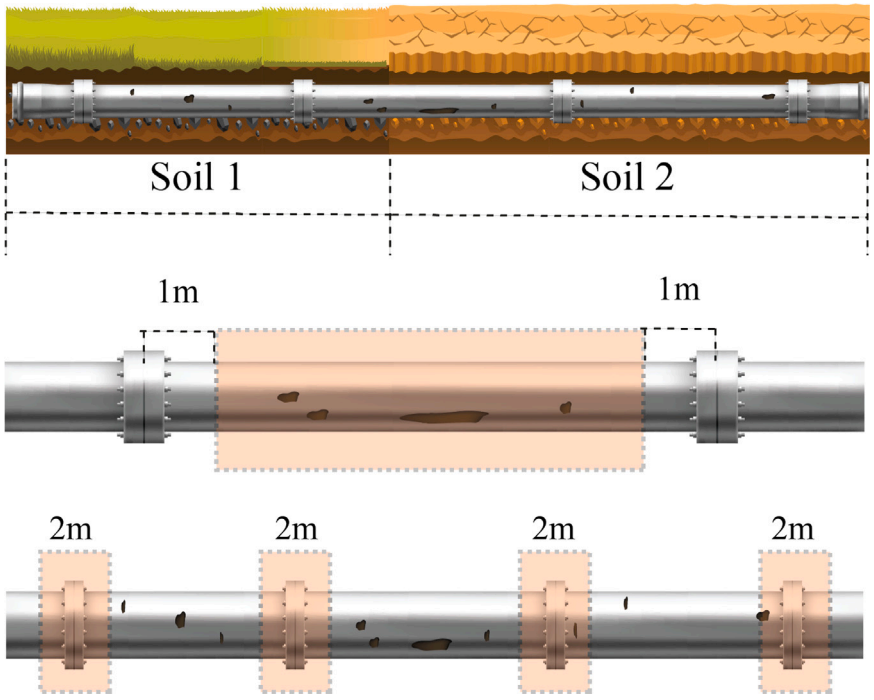

Fig. 7. Scheme of the three main analysis, using flanges to represent the welding joints.

Table 6
Summary results for the CSR tests for the inner wall of the *new* defects.

Soil	S1	S2	S1	S3	S4	S5	S6	S5	S6	S7	S6	S7	S4	UZ	S5	S4	S7	UZ
No.	1228	2335	1955	2686	2246	1700	919	2147	966	316	1344	19	692	663	1939	1240	1271	5419
CE	0.025	0.025	0.025	0.025	0.025	0.025	0.025	0.025	0.025	0.025	0.025	NA	0.025	0.025	0.025	0.025	0.025	0.025
TH	0.025	0.025	0.025	0.025	0.025	0.025	0.025	0.025	0.025	0.025	0.025	NA	0.025	0.025	0.025	0.025	0.025	0.025
BE	0.082	0.05	0.062	0.055	0.054	0.055	0.043	0.049	0.067	0.07	0.087	NA	0.05	0.039	0.062	0.046	0.073	0.046
BY	0.025	0.025	0.025	0.025	0.025	0.025	0.025	0.025	0.025	0.025	0.025	NA	0.025	0.025	0.025	0.025	0.025	0.025
DC	0.025	0.025	0.025	0.025	0.025	0.025	0.025	0.025	0.025	0.025	0.025	NA	0.025	0.025	0.025	0.025	0.025	0.025
MD	0.025	0.025	0.025	0.025	0.025	0.025	0.025	0.025	0.025	0.025	0.025	NA	0.025	0.025	0.025	0.025	0.025	0.025

S1: Soil 1, S2: Soil 2, S3: Sol 3, S4: Soil 4, S5: Soil 5, S6: Soil 6, S7: Soil 7, UZ: Urban Zone
CE: Clark & Evans test, TH: Thompson test, BE: Besag & Gleaves test, BY: Byth & Ripley test, MD: Maximum Deviation (MAD)
DC: Diggle–Cressie–Loosmore–Ford (DCLF) test
Green: Clustered distribution, Yellow: Random distribution, No.: Number of defects per category, NA: Not applicable.

Table 7
Summary results for the CSR tests for the outer wall of the *new* defects.

Soil	S1	S2	S1	S3	S4	S5	S6	S5	S6	S7	S6	S7	S4	UZ	S5	S4	S7	UZ
No.	202	0	47	49	2	4	24	5	1	0	1	0	5	132	26	52	1696	304
CE	0.025	NA	0.025	0.025	NA	NA	0.025	NA	NA	NA	NA	NA	NA	0.26	0.172	0.104	0.065	0.025
TH	0.025	NA	0.025	0.025	NA	NA	0.025	NA	NA	NA	NA	NA	NA	0.025	0.025	0.025	0.025	0.025
BE	0.112	NA	0.027	0.08	NA	NA	0.027	NA	NA	NA	NA	NA	NA	0.18	0.097	0.18	0.146	0.095
BY	0.025	NA	0.025	0.025	NA	NA	0.025	NA	NA	NA	NA	NA	NA	0.025	0.025	0.025	0.025	0.025
DC	0.025	NA	0.025	0.025	NA	NA	0.025	NA	NA	NA	NA	NA	NA	0.025	0.025	0.025	0.025	0.025
MD	0.025	NA	0.025	0.025	NA	NA	0.025	NA	NA	NA	NA	NA	NA	0.025	0.025	0.025	0.025	0.025

S1: Soil 1, S2: Soil 2, S3: Sol 3, S4: Soil 4, S5: Soil 5, S6: Soil 6, S7: Soil 7, UZ: Urban Zone
CE: Clark & Evans test, TH: Thompson test, BE: Besag & Gleaves test, BY: Byth & Ripley test,
DC: Diggle–Cressie–Loosmore–Ford (DCLF) test, MD: Maximum Deviation (MAD)
Green: Clustered distribution, Yellow: Random distribution, No.: Number of defects per category, NA: Not applicable.

the Besag & Gleaves was discarded because, again, it failed to reject the CSR assumption, suggesting that this method has some possible biases for this purpose. Instead of using the Euclidean distance in the unwrapped plane, the Besag & Gleaves method might be used to calculate the nearest neighbor distance considering a cylinder geodesic. This case, however, was not taken into consideration in this work and will be contemplated in subsequent works.

The following analyses centered on the mean behavior of the segments between contiguous welding joints. The segments without 1 m apart from the weld joints were used for the first analysis, and the segments 1 m apart on each side of the weld joints were used in the second analysis (Table 8). The results shown in this table suggest some exciting trends. On the one hand, Clark & Evans and the functional methods (i.e., DCLF and MAD) suggested a random distribution for the segments without the welds. The Thompson and the Byth & Ripley (nearest distance-based) tests, on the other hand, revealed clustered point patterns. Regarding the segment in the joint welds, clustered and random distributions were obtained, with the former having a

Table 8
Summary results for the CSR tests for the *new* defects between joints in the inner wall.

Set	Soil	S1	S2	S1	S3	S4	S5	S6	S5	S6	S7	S6	S7	S4	UZ	S5	S4	S7	UZ
Seg. Joints	CE	0.31	0.31	0.25	0.31	0.28	0.24	0.26	0.32	0.36	0.21	0.3	0.34	0.36	0.17	NA	0.31	0.235	0.27
	TH	0.03	0.03	0.03	0.03	0.03	0.03	0.03	0.03	0.03	0.03	0.03	0.03	0.03	0.03	NA	0.03	0.03	0.03
	BY	0.03	0.03	0.03	0.03	0.03	0.03	0.03	0.03	0.03	0.03	0.03	0.03	0.03	0.03	NA	0.03	0.03	0.03
	DC	0.08	0.27	0.13	0.26	0.28	0.28	0.17	0.25	0.21	0.19	0.14	0.27	0.25	0.04	NA	0.22	0.19	0.20
	MD	0.09	0.27	0.1	0.26	0.27	0.27	0.13	0.21	0.19	0.16	0.15	0.22	0.16	0.03	NA	0.22	0.231	0.19
1m Welds	CE	0.37	0.14	0.33	0.22	0.28	0.46	NA	0.37	0.16	0.03	NA	NA	0.51	NA	NA	0.08	0.1	0.14
	TH	0.03	0.03	0.03	0.03	0.03	0.03	NA	0.03	0.03	0.03	NA	NA	0.03	NA	NA	0.03	0.025	0.03
	BY	0.03	0.03	0.03	0.03	0.03	0.03	NA	0.03	0.03	0.03	NA	NA	0.03	NA	NA	0.03	0.025	0.03
	DC	0.11	0.24	0.4	0.2	0.48	0.62	NA	0.06	0.1	0.05	NA	NA	0.1	NA	NA	0.24	0.05	0.08
	MD	0.05	0.05	0.5	0.22	0.44	0.03	NA	0.23	0.14	0.04	NA	NA	0.05	NA	NA	0.09	0.08	0.06

S1: Soil 1, S2: Soil 2, S3: Sol 3, S4: Soil 4, S5: Soil 5, S6: Soil 6, S7: Soil 7, UZ: Urban Zone
CE: Clark & Evans test, TH: Thompson test, BE: Besag & Gleaves test, BY: Byth & Ripley test, MD: Maximum Deviation (MAD)
DC: Diggle–Cressie–Loosmore–Ford (DCLF) test
Green: Clustered distribution, Yellow: Random distribution, NA: Not applicable.

Table 9
Nearest neighbor ratio results for the deterministic and Binomial expected distances.

Analysis	Data	Deterministic ratio									Binomial ratio								
		Pipe	S1	S2	S3	S4	S5	S6	S7	UZ	Pipe	S1	S2	S3	S4	S5	S6	S7	UZ
Complete set	ILI1Int	0.28	0.6	0.23	0.13	0.27	0.31	0.21	0.59	0.21	0.17	0.24	0.17	0.05	0.16	0.22	0.12	0.28	0.14
	ILI2Int	0.61	0.78	0.44	0.49	0.55	0.47	0.6	0.65	0.35	0.45	0.47	0.37	0.40	0.42	0.39	0.45	0.37	0.26
	ILI1Ext	1.35	3.42	NR*	0.83	3.68	0.06	29.8	20.3	0.91	0.25	0.58	NR	0.07	0.29	0.00	1.47	10.4	0.16
	ILI2Ext	1.19	2.4	NR	1.7	6.64	0.18	0.03	0.3	1.57	0.28	0.50	NR	0.21	0.67	0.12	0.00	0.20	0.31
Segments-without 1m welds	ILI1Int	1.08	1.6	0.96	0.95	1	1.02	1.01	1.17	0.94	0.83	0.78	0.87	0.87	0.87	0.87	0.84	0.79	0.81
	ILI2Int	1.06	1.2	1.12	1.03	0.99	1.08	0.98	1.03	0.95	0.78	0.70	0.86	0.81	0.76	0.85	0.76	0.75	0.79
	ILI1Ext	0.95	1.33	NR	0.97	0.85	1.26	1.41	0.74	0.68	0.53	0.60	NR	0.86	0.59	0.66	0.93	0.55	0.42
	ILI2Ext	1.05	1.43	NR	1.01	1.25	1.26	0.58	0.83	0.58	0.55	0.61	NR	0.66	0.67	0.58	0.50	0.69	0.37
Welds up to 1m	ILI1Int	0.73	0.71	0.69	0.77	0.74	0.78	0.67	0.73	0.72	0.58	0.57	0.55	0.61	0.57	0.63	0.53	0.60	0.56
	ILI2Int	0.84	0.89	0.83	0.9	0.85	0.78	0.85	0.91	0.78	0.65	0.68	0.67	0.69	0.64	0.62	0.64	0.73	0.62
	ILI1Ext	0.64	0.68	NR	0.88	1.25	0.15	0.45	0.72	0.57	0.46	0.47	NR	0.53	0.75	0.12	0.35	0.61	0.40
	ILI2Ext	0.76	0.65	NR	0.87	0.77	1.32	0.39	0.81	0.76	0.56	0.46	NR	0.58	0.54	0.91	0.32	0.71	0.52

S1: Soil 1, S2: Soil 2, S3: Sol 3, S4: Soil 4, S5: Soil 5, S6: Soil 6, S7: Soil 7, UZ: Urban Zone
ILI1Int and ILI2Int are the first and second ILI runs datasets at the inner wall dataset, respectively.
ILI1Ext and ILI2Ext are the first and second ILI runs datasets at the outer wall dataset, respectively.
*NR: No defects reported.
S1: Soil 1, S2: Soil 2, S3: Soil 3, S4: Soil 4, S5: Soil 5, S6: Soil 6, S7: Soil 7, S8: Near urban zone.
Green: Clustered distribution, Yellow: Random distribution, Red: Dispersed distribution

higher proportion. On the basis of the previously stated, it may also be considered a random position between consecutive inspections and higher clustering near the joint welds.

6.1.2. Results for CSR tests applied to defects with $d \leq 15\%t$

As previously stated, most corrosion depths fall between 10 and 12%t. This section presents the results for *new* defects with a depth smaller than 15%t. The statistic of Clark & Evans (nearest neighbor ratio) is calculated for the aforementioned cases solely for illustration. This ratio was also calculated using a random binomial process, which compares the mean nearest distance under the CSR assumption by imposing the number of random points. The results in Table 9 show patterns consistent with those previously mentioned. The defects tend to have a cluster distribution, the results of the segments were close to the random mean nearest distance (i.e., statistic close to 1), and the defects near the welds tend to be more clustered (statistic < 1). Although some dispersed distributions (ratio > 1) can be obtained in this situation, they are only connected to a small number of defects, making it impossible to predict the outcomes thoroughly. The findings suggest corrosion defects do not follow a CSR distribution along the whole pipeline. Despite the possibility of them occurring randomly between weld joints, defects close to the welding joints and the Heat-Affected-Zone (HAZ) would impact this assumption.

It should be noted that the Clark & Evans test was used to determine the results in Table 9 and that the Monte Carlo method was not contemplated in this case. Following the Monte Carlo rank, the CSR was assessed, and again, the results showed a predominant cluster pattern in which none of the segments indicated a dispersed distribution. Similar classifications to those presented in Table 8 were obtained for the segments between consecutive inspections.

6.2. Interaction of new defects

The permutation test of the cross-K function with $M = 99$ simulations was implemented with a maximum distance lag of 0.42 m to avoid edge effects in the circumferential direction (i.e., half the perimeter). The second inspection is not contemplated because it includes additional defects that are not identified yet, requiring further matching with another ILI measurement. The results for each of the registers at the inner and outer walls are displayed in Fig. 8. This figure indicates that both pipe walls exhibit repulsion for $h \leq 5$ mm, meaning that *old* defects have fewer surrounding *new* defects than expected. Sections with few *old* defects, such as isolated corrosion sites or previous clusters of *old* points, can have an impact on the repulsion distance.

The results are comparable when Deep and Shallow defects are taken into account. In this case, it is assumed that Deep defects have a depth $d \geq 25\%t$ and Shallow defects have a depth of $d \leq 25\%t$ (Fig. 9). In contrast to the earlier findings, the repulsion is predicted to occur after a separation of $h \geq 20$ mm in both pipe walls (instead of $h \geq 5$ mm). This outcome is expected since the *old* dataset includes several defects with depths under $25\%t$ that cluster with both shallow and deep corrosion points. This figure also depicts a more "random" or expected behavior for lags larger than 20 mm, which is primarily represented by the amount and distribution of the shallow defects. Since shallow defects account for over 90% of the reported data in this case, deep defects would have a greater proportion of shallow

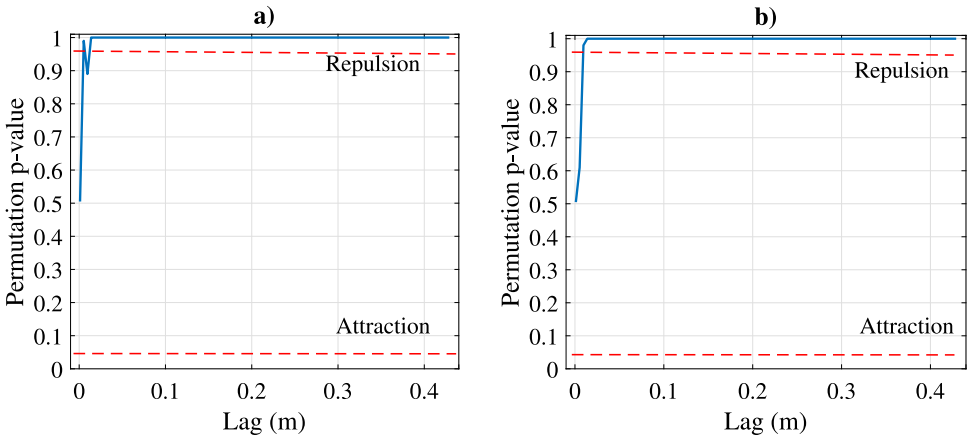

Fig. 8. Permutation test results for the (a) inner and (b) outer walls.

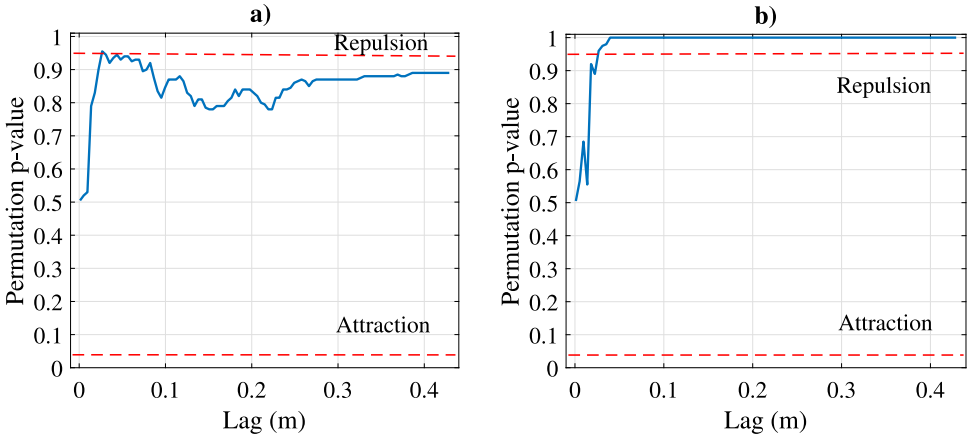

Fig. 9. Permutation test results for deep vs shallow defects for the (a) inner and (b) outer walls.

neighbors. The indistinguishable behavior of the inner wall is explained by the fact that these cross neighbors have shorter separations than in the case of *old* and *new* records. Although shallow and deep defects are separated in a similar way at the outer wall, comparable to that of the inner wall, there are significantly fewer shallow points, promoting isolated deep defects and the repulsion influence.

The interaction of *old* and *new* defects was assessed for each type of soil based on the permutation test; these findings are displayed in Table 10. According to this table, every soil type exhibits a predominant repulsion interaction at the inner and outer walls. The exceptions occurred in soil S3, which exhibits an attraction ($h \geq 300$ mm), and soil S6, with more random expected behavior at the outer wall. S3 is an extremely-to-strong acid soil with sandy clastic rocks and clay silt, which may adhere to the outer wall and facilitate attraction. S6 corresponds to terraces with poor to moderately drained soil and extremely-to-neutral acid soil. These varied conditions could explain a more random pattern. For the inner wall, the repulsion influence distance ranges from 13 to 26 mm, and for the outer wall, it ranges from 9.55 to 40 mm. Both populations have similar mean nearest-neighbor distances of around 180 mm.

So far, the results have shown the full pipeline segment, but other results may occur on a lower evaluation scale. In this regard, the interaction test was used for every joint having at least ten corrosion points for each population. Although specific results were obtained for each pipe joint, the overall distribution of how the outcomes can be classified into Attraction, Repulsion, or Random interactions is shown in Fig. 10. According to this figure, all joints initially interact randomly over shorter distances, and the proportion of repulsion increases after 50 mm. Also, according to this figure, less than 5% of joints show an attraction in different lags, but they mainly occur in the inner rather than the outer wall. These results confirm that corrosion defects exhibit a strong repulsion effect, which may be due to an initial electrochemical inhibition from the *old* corrosion points. Note that this analysis considered only the center of the corrosion points and not their length and width, as depicted in Fig. 1. According to many authors, the radio of corrosion pits is expected to increase as corrosion progresses, possibly leading to a coalescence that is also favored by nearby cracks [53–55].

6.3. Simulation of new defects

The bandwidth for the kernel smoothing was compared based on different approaches. They include the Mean Square Error Cross-validated method of Diggle [47], the likelihood Cross-validation method of Loader [45], the non-parametric method of Cronie & Van Lieshout [46], and the rule of thumb reported by Scott [48]. For all cases, a Gaussian Kernel with the Diggle edge correction was considered. Many authors commonly prefer the Gaussian Kernel, and Baddeley [42] remarked that the Diggle correction had a better performance. For the comparison, the intensity values are computed only at the points using a leave-one-out approach, where all the points except the one being estimated contribute to the kernel smoothing. Given $x_1, \ldots, x_n$ measurements, the intensity at each point is given by:

$$\tilde{\lambda}(x_i) = \sum_{j \neq i} \frac{1}{e(x_j)} \mathcal{K}(x_j - x_i) \tag{10}$$

Based on the above, standard errors were obtained and compared for each case to provide an idea of the accuracy of the methods. It followed the method implemented by Baddeley [42] in the package

Table 10
Influence results by type of soil.

Soil category	ILI1-Int		ILI1-Ext		Mean NN distance (m)	
	Influence	Lag (m)	Influence	Lag (m)	ILI1-Int	ILI1-Ext
S1	Repulsion	0.0224	Repulsion	0.014	0.1771	0.1607
S2	Repulsion	0.0138	–	NA	0.1850	NA
S3	Repulsion	0.0267	Attraction	0.301	0.1927	0.2342
S4	Repulsion	0.0181	Repulsion	0.040	0.1780	0.2413
S5	Repulsion	0.0138	–	NA	0.1816	NA
S6	Repulsion	0.0224	Random	0.4	0.1729	0.1400
S7	Repulsion	0.0138	Repulsion	0.010	0.1478	0.1885
UZ	Repulsion	0.0138	Repulsion	0.018	0.1671	0.1538

NN: Nearest Neighbor, NA: Non data available.

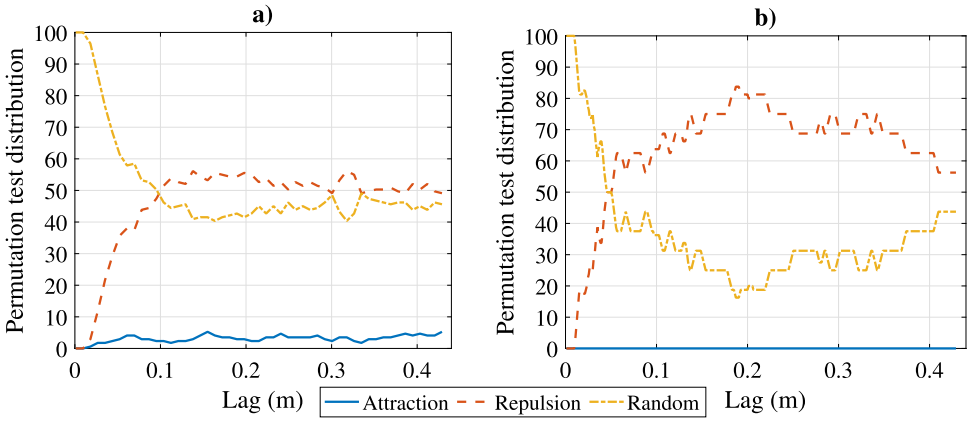

Fig. 10. Distribution of the permutation test for the (a) inner and (b) outer walls.

Table 11
Bandwidth results for different criteria for kernel fitting.

Dataset	Criterion	Min	Q_1	Q_2	Mean	Q_3	Max
ILI1-Int	Diggle	0.00E+00	2.30E−04	2.03E+00	1.33E+01	2.34E+01	1.09E+02
	Loader	0.00E+00	7.09E−02	8.57E−02	8.69E−02	9.91E−02	1.62E−01
	Scott	2.73E−03	1.22E−02	1.42E−02	1.46E−02	1.69E−02	2.49E−02
	CvL	0.00E+00	2.63E−01	3.25E−01	3.30E−01	3.86E−01	7.02E−01
ILI2-Int	Diggle	0.00E+00	1.89E−02	4.41E+00	1.41E+01	2.52E+01	1.18E+02
	Loader	0.00E+00	1.34E−02	1.69E−02	1.66E−02	1.99E−02	2.70E−02
	Scott	2.11E−03	2.71E−02	3.22E−02	3.29E−02	3.83E−02	7.01E−02
	CvL	0.00E+00	6.23E−01	8.12E−01	8.08E−01	1.01E+00	1.65E+00
ILI1-Ext	Diggle	0.00E+00	5.00E−05	1.18E+01	2.34E+01	4.29E+01	1.06E+02
	Loader	0.00E+00	3.06E−03	6.89E−03	9.11E−03	1.54E−02	1.60E−02
	Scott	5.22E−04	3.99E−03	5.82E−03	6.31E−03	9.23E−03	1.04E−02
	CvL	0.00E+00	4.65E−02	9.37E−02	9.88E−02	1.63E−01	2.02E−01
ILI2-Ext	Diggle	0.00E+00	1.61E−02	1.03E+01	1.83E+01	3.38E+01	1.04E+02
	Loader	0.00E+00	1.66E−03	8.98E−03	6.26E−03	9.47E−03	9.61E−03
	Scott	9.23E−04	7.53E−03	1.41E−02	1.35E−02	1.94E−02	2.14E−02
	CvL	0.00E+00	1.05E−01	2.72E−01	2.28E−01	3.39E−01	3.98E−01

*Q_1, Q_2, and Q_3 are the first, second and third quartiles of the data, respectively.

spatstat of R. According to Baddeley, the variance of $\tilde{\lambda}(u)$ can be obtained assuming a Poisson Process with isotropic Gaussian kernel. The results for each bandwidth selection method are summarized in Table 11. This table depicts the standard error's minimum, mean, and quartiles (i.e., Q_1−25%, Q_2−50%, Q_3−75%) measurements. The results show that the Diggle selection method had higher errors, which could be associated with the inherent assumption of a Cox Process, i.e., a realization of a stochastic process. The lower errors were obtained for the Loader's approach and Scott's rule of thumb, but as mentioned before, this rule of thumb does not depend on the location, and an over-smooth intensity is expected. Therefore, the likelihood cross-validation method of Loader was selected.

The main idea behind the Inhomogeneous intensity is to simulate the location of new defects more appropriately. Consider the $\tilde{\lambda}(x)$ obtained for the defects not matched in the first inspection and the location of the new defects reported in the second one. The new defects in the second inspection are expected to appear in a higher proportion in those locations where $\tilde{\lambda}(x)$ has high values. In this regard, both results for the inner and the outer walls were compared in Figs. 11 and 12, considering a log-normal scale and white crosses for locations of *new* points.

The results show an agreement in the predominant location of the defects, as it can be easily identified for the outer wall near kilometers 10, 27, and 33. However, these figures also depict some locations that were not very likely to appear at a corrosion point. However, these figures display both inhomogeneous densities and are not associated with a specific probability, so it cannot be affirmed how probable these locations would be. Additional smoothing approaches can be considered using an adaptive perspective to prevent low-intensity areas from being under-smoothed and high values from having excessive

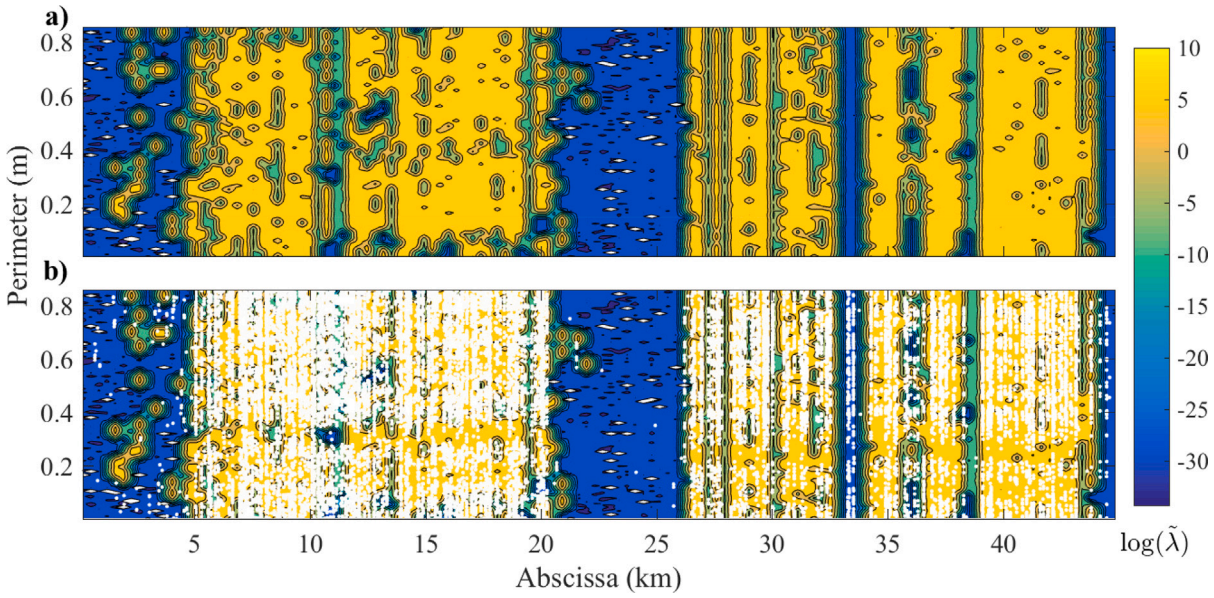

Fig. 11. Obtained $\tilde{\lambda}(x)$ for ILI1-Int (a) without new defects in ILI2-Int and (b) including the new defects in ILI2-Int.

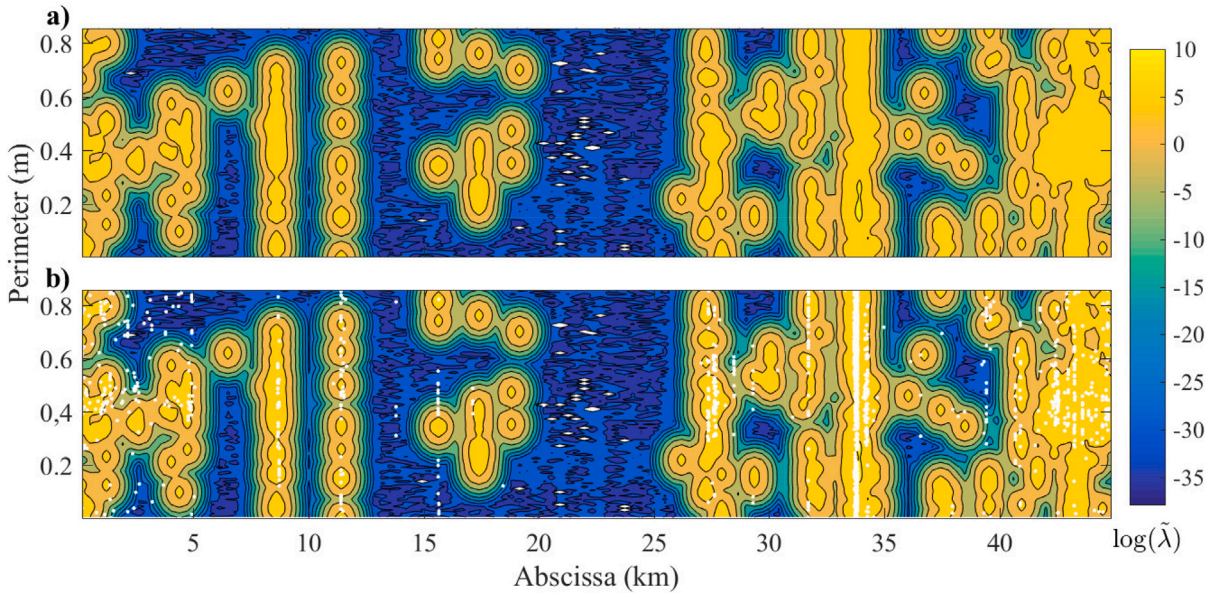

Fig. 12. Obtained $\tilde{\lambda}(x)$ for ILI1-Ext (a) without new defects in ILI2-Ext and (b) including the new defects in ILI2-Ext.

over-smoothed results. For this purpose, adaptive estimators using the Voronoi tessellation could be considered [42].

7. Conclusions

In the paper, a framework for analyzing and simulating *new* corrosion defects is presented. Based on the test for Complete Spatial Randomness (CSR) assumption, the framework includes an analysis of the spatial distribution of the defects. This approach also assesses the interaction between *new* and *old* defects that were initially identified using a matching approach. Lastly, it suggests the Non-Homogeneous Poisson Process (NHPP) as an alternative for simulating the location of new defects appearing between inspections. The main findings are:

1. The CSR assumption was evaluated using six different methods. The results suggested that the *new* defects follow a clustered distribution for each type of soil and pipe wall. This pattern was also identified for the defects close to the welding joints. However, after applying the test for segments between welding joints (without the 1 m apart of the weld joints), some tests failed to reject the CSR assumption (i.e., they accept the uniform random distribution). The cluster pattern was expected considering the formation of pitting and localized attack, for instance, near the pipe welds in the Heat-Affected Zone. A bigger evaluation window may lead to more dispersed areas failing the CSR tests. However, as reported by Valor et al. [56], the corrosion patterns focused almost entirely on a cluster and random patterns (in a lower proportion). Lastly, comparing the six methods, it was obtained that the Besag & Gleaves method may fail to identify cluster point patterns, so it should be considered cautiously. If a cylinder geodesic is considered to determine the nearest neighbor distance, the Besag & Gleaves test results could obtain better results based on how the T-square sampling is constructed.

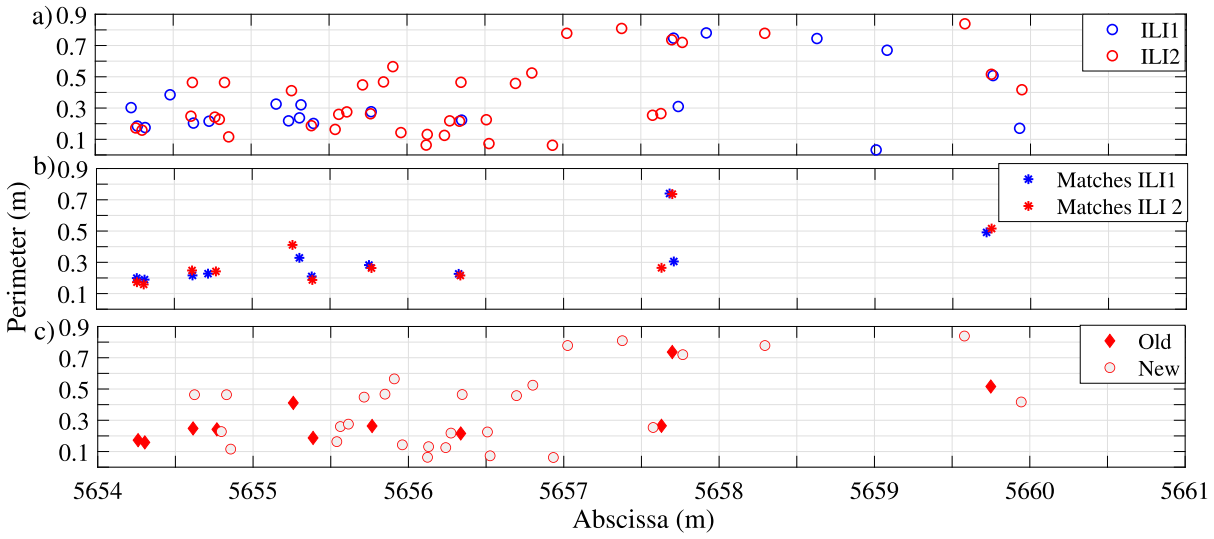

Fig. A.13. (a) Initial ILI data; (b) matches by the matching approach, and (c) obtained *new* and *old* datasets. *Source:* Adapted from [23].

2. The random-permutation test was evaluated to determine if the *new* and *old* defects can be considered indistinguishable or if they tend to follow a repulsion or an attraction pattern. The results showed a predominant repulsion between the two sets, especially after a separation of 50 mm. This paper also analyzed shallow ($d \leq 25\%t$) and deep ($d > 25\%t$) defects, obtaining a similar tendency.
3. Different methods to estimate bandwidth for the inhomogeneous smoothing kernel were compared. They included cross-validation approaches, non-parametric methods, and the rule of thumb reported by Scott [48]. This study considered the likelihood cross-validation method reported by Loader [45] given its low standard error in the estimate at the points. This paper illustrated how the distribution between the *new* defects in the first and second inspections are closely located. Typically, a Homogeneous Poisson Process is implemented to simulate the random location of new corrosion points. Still, the approach proposed in this work suggests an interesting alternative that contemplates possible clusters and dispersed locations. This alternative would help generate new defects in further reliability analysis compared to those following a Complete Spatial Randomness.

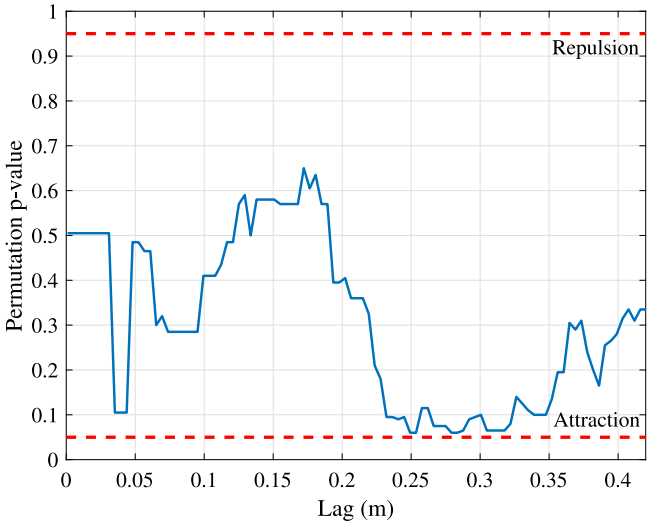

Fig. A.14. Obtained results for the repulsion and attraction test for the application example.

CRediT authorship contribution statement

Rafael Amaya-Gómez: Writing – review & editing, Writing – original draft, Visualization, Validation, Software, Resources, Methodology, Investigation, Formal analysis, Data curation, Conceptualization. **Mauricio Sánchez-Silva:** Writing – review & editing, Resources, Methodology, Conceptualization. **Felipe Muñoz:** Writing – review & editing, Resources, Methodology, Conceptualization. **Franck Schoefs:** Writing – review & editing, Resources, Conceptualization. **Emilio Bastidas-Arteaga:** Writing – review & editing, Resources, Methodology, Conceptualization.

Declaration of competing interest

The authors declare that they have no known competing financial interests or personal relationships that could have appeared to influence the work reported in this paper.

Data availability

The authors do not have permission to share data.

Acknowledgments

R. Amaya-Gómez thanks the National Department of Science, Technology and Innovation of Colombia for the Ph.D. scholarship (COLCIENCIAS Grant No. 727, 2015) and Campus France for the Eiffel Excellence Program (2018).

Appendix. Application example

To illustrate how the proposed framework can be applied, consider the example reported in the matching approach of Amaya-Gómez et al. [23]. This example contemplates 21 and 39 corrosion defects in the first and second inspections, respectively, between 5654 and 5661 m of the pipe abscissa, as shown in Fig. A.13a. Following the matching approach, eleven matches were determined that are depicted in Fig. A.13b, which allow us to discriminate between *new* and *old* corrosion points in the last ILI measurement in Fig. A.13c.

Considering the *new* dataset, it was implemented the CSR tests of Clark & Evans, Thompson, Byth & Ripley, Diggle–Cressie–Loosmore–Ford (DCLF), and Maximum Deviation (MAD). The obtained results are

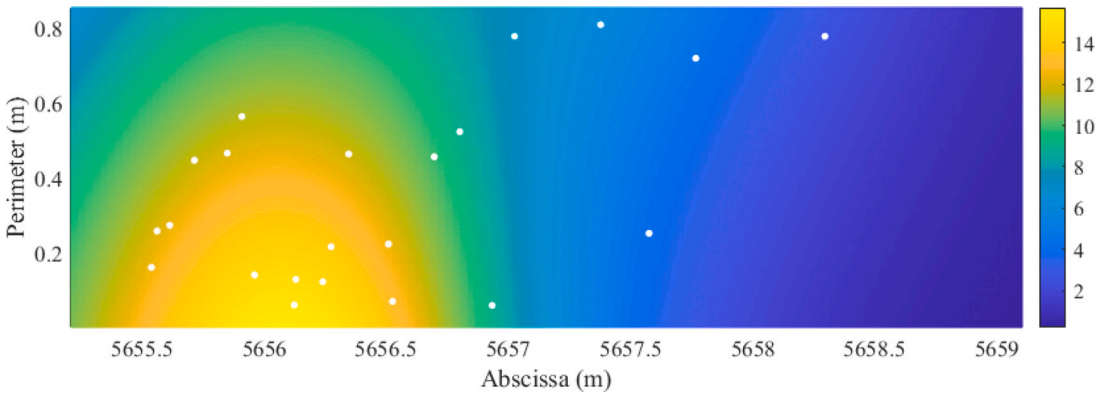

Fig. A.15. Obtained $\tilde{\lambda}(x)$ for the application example, including the location of new defects with white markers.

Table A.12
CSR test results for the application example.

Test	p-value (Clustered)
Clark & Evans	0.25
Thompson	0.01
Byth & Ripley	0.01
Diggle–Cressie–Loosmore–Ford (DCLF)	0.05
Maximum Deviation (MAD)	0.07

Green: Clustered distribution, Yellow: Random distribution.

shown in Table A.12, after removing 1 m to the welds from each side, i.e., the final segment starts from 5655 to 5660 m. These results suggest that Clark & Evans and the MAD tests fail to reject the null hypothesis of the CSR assumption and that the remaining suggest a more clustered distribution. These p-values were determined following the equations of Table 1 with $n = 28$, contemplating the R-project functions of the *spatstat* package *clarkevans.test*, *dclf.test*, and *mad.test*.

Let us take the Clark & Evans statistic and its significance test for illustrative purposes. First, it is necessary to estimate the parameters $\mathbb{E}_r$ and σ_r, considering the study area $A = 3.36$ m^2, the perimeter is $P_e = 9.56$ m and $n = 28$, which follows that $\mathbb{E}_r = 0.222$ and $\sigma_r = 0.0278$. Then, using the mean nearest neighbor distance for each point in the *new* dataset follows that $CE_D = 0.90$. Based on a Monte Carlo test approach, with 99 equally-sized random point patterns under a ranking perspective, as mentioned in Section 2, it was obtained a p-value of 0.25. This result indicates that the CSR assumption cannot be rejected with a significance level of 0.05, which is confirmed by the statistic close to the unity and the p-value greater than the rejection zone.

Considering both the *new* and *old* points (Fig. A.13c), the Smith [38] approach first creates a function for computing a vector distinct pairwise distances, then the K_{ON} cross function using a permutation perspective using count point frequencies and a counting rule for finding $d_{ON}(i, j)$ in the vector of distances. Finally, this approach compares the *new* and *old* defects using a random permutation for different lag distances. Further details are explained in Ref. [38]. The results of this approach are depicted in Fig. A.14, where it can be noted an attraction of the *new* after 0.25 m, which makes sense taking into account the clustered result of some CSR tests and the fact in Fig. A.13c they are closely located to the *old* ones.

Finally, using the non-homogeneous kernel density estimation function of R-project *density* of the *stats* package, with the Loader's bandwidth criterion, it was obtained the results depicted in Fig. A.15. This figure shows the areas of the segment where more simulated defects would appear under an Inhomogeneous Poisson Point Process, which aims to address the clustered (and attraction interaction) of the *new* corrosion points given the previous results.

References

[1] Amaya-Gómez R, Bastidas-Arteaga E, Muñoz F, Sánchez-Silva M. Statistical soil characterization of an underground corroded pipeline using in-line inspections. Metals 2021;11(2).
[2] Castaneda H, Rosas O. External corrosion of pipelines in soil. In: Oil and gas pipelines. John Wiley & Sons, Ltd; 2015, p. 265–74.
[3] Yazdi M, Khan F, Abbassi R, Quddus N, Castaneda-Lopez H. A review of risk-based decision-making models for microbiologically influenced corrosion (MIC) in offshore pipelines. Reliab Eng Syst Saf 2022;223:108474.
[4] Zhang N, Zeng D, Zhang Z, Zhao W, Yao G. Effect of flow velocity on pipeline steel corrosion behaviour in H2S/CO2 environment with sulphur deposition. Corros Eng Sci Technol 2018;53(5):370–7.
[5] Kim C, Chen L, Wang H, Castaneda H. Global and local parameters for characterizing and modeling external corrosion in underground coated steel pipelines: A review of critical factors. J Pipeline Sci Eng 2021;1(1):17–35, Special Issue on Pipeline Corrosion and Its Management.
[6] Amaya-Gómez R, Sánchez-Silva M, Bastidas-Arteaga E, Schoefs F, Muñoz F. Reliability assessments of corroded pipelines based on internal pressure – A review. Eng Fail Anal 2019;98:190–214.
[7] Ramírez-Camacho JG, Carbone F, Pastor E, Bubbico R, Casal J. Assessing the consequences of pipeline accidents to support land-use planning. Saf Sci 2017;97:34–42.
[8] Yarveisy R, Khan F, Abbassi R. Data-driven predictive corrosion failure model for maintenance planning of process systems. Comput Chem Eng 2022;157:107612.
[9] Khan F, Yarveisy R, R. Abbassi. Risk-based pipeline integrity management: A road map for the resilient pipelines. J Pipeline Sci Eng 2021;1(1):74–87, Special Issue on Pipeline Corrosion and Its Management.
[10] POF. Specifications and requirements for intelligent pig inspection of pipelines. Technical report, Pipeline Operators Forum; 2008.
[11] Amaya-Gómez R, Riascos-Ochoa J, Muñoz F, Bastidas-Arteaga E, Schoefs F, Sánchez-Silva M. Modeling of pipeline corrosion degradation mechanism with a Lévy Process based on ILI (In-Line) inspections. Int J Press Vessels Pip 2019;172:261–71.
[12] Siraj T, Zhou W. Quantification of measurement errors in the lengths of metal-loss corrosion defects reported by inline inspection tools. J Pressure Vessel Technol 2019;141(6). 061402.
[13] Straub D. Generic approaches to risk based inspection planning for steel structures (Ph.D. thesis), Institute of Structural Engineering, ETH Zurich; 2004.
[14] Amaya-Gómez R, Sánchez-Silva M, Muñoz F. Pattern recognition techniques implementation on data from In-Line Inspection (ILI). J Loss Prev Process Ind 2016;44:735–47.
[15] Zhang S, Zhou W. Cost-based optimal maintenance decisions for corroding natural gas pipelines based on stochastic degradation models. Eng Struct 2014;74:74–85.
[16] Miran SA, Huang Q, Castaneda H. Time-Dependent reliability analysis of corroded buried pipelines considering external defects. J Infrastruct Syst 2016;22(3):04016019.
[17] Dzioyev KM, Basiyev KD, Khabalov GI, Dzarukayev EV. Stress corrosion processes in the metal and welded joints in gas pipelines. Weld Int 2014;28(9):717–21.
[18] Khan F, Yarveisy R, Abbassi R. Cross-country pipeline inspection data analysis and testing of probabilistic degradation models. J Pipeline Sci Eng 2021;1(3):308–20, Special Issue on Risk and Reliability Assessment of Pipelines.
[19] Benjamin AC, Freire JLF, Vieira RD. Part 6: Analysis of pipeline containing interacting corrosion defects. Exp Tech 2007;31(3):74–82.
[20] Winkelmann R. Seemingly unrelated negative binomial regression. Oxf Bull Econ Stat 2000;62(4):553–60.

[21] Chib S, Winkelmann R. Markov chain Monte Carlo analysis of correlated count data. J Bus Econom Statist 2001;19(4):428–35.
[22] Wang X, Wang H, Tang F, Castaneda H, Liang R. Statistical analysis of spatial distribution of external corrosion defects in buried pipelines using a multivariate Poisson-lognormal model. Struct Infrastr Eng 2020;1–16.
[23] Amaya-Gómez R, Sánchez-Silva M, Muñoz F, Bastidas-Arteaga E, F. Schoefs. Matching of corroded defects in onshore pipelines based on In-Line Inspections and Voronoi partitions. Working paper, 2020.
[24] Moller J, Waagepetersen RP. Statistical inference and simulation for spatial point processes. Chapman & Hall/CRC monographs on statistics & applied probability, CRC Press; 2003.
[25] Szmyt J. Spatial statistics in ecological analysis: From indices to functions. Silva Fennica 2014;48(1).
[26] Ripley BD. Tests of 'randomness' for spatial point patterns. J R Stat Soc Ser B Stat Methodol 1979;41(3):368–74.
[27] Thompson HR. Distribution of distance to nth neighbour in a population of randomly distributed individuals. Ecology 1956;37(2):391–4.
[28] Byth K, Ripley BD. On sampling spatial patterns by distance methods. Biometrics 1980;36(2):279–84.
[29] Besag J, Gleaves JT. On the detection of spatial pattern in plant communities. Bull Int Stat Inst 1973;45(1):153–8.
[30] Dettloff KE. A review and evaluation of classical nearest-neighbor tests in ecology for detecting non-randomness in 2-D spatial point patterns. Technical report, Oregon State University; 2014.
[31] Assunção R. Testing spatial randomness by means of angles. Biometrics 1994;50(2):531–7.
[32] Abousamra S, Gupta R, Kurc T, Samaras D, Saltz J, Chen C. Topology-guided multi-class cell context generation for digital pathology. In: Proceedings of the IEEE/CVF conference on computer vision and pattern recognition. 2023, p. 3323–33.
[33] Dixon PM. Ripley's K function. In: El-Shaarawi AH, Piegorsch WW, editors. Encyclopedia of environmetrics. John Wiley; 2002, p. 1796–803.
[34] Baddeley A, Diggle PJ, Hardegen A, Lawrence T, Milne RK, Nair G. On tests of spatial pattern based on simulation envelopes. Ecol Monograph 2014;84(3):477–89.
[35] Department of the Navy Bureau of Yards, Docks US. Corrosion prevention and control. NAVDOCKS, U.S. Government Printing Office; 1965.
[36] Cressie NAC. Statistics for spatial data. John Wiley & Sons, Inc; 1993.
[37] Diggle PJ, Cox TF. On sparse sampling methods and tests of independence for multivariate spatial point patterns. Bull Int Stat Inst 1981;49:213–29.
[38] Smith TE. A scale-Sensitive test of attraction and repulsion between spatial point patterns. Geograph Anal 2004;36(4):315–31.
[39] Lotwick HW, Silverman BW. Methods for analysing spatial processes of several types of points. J R Stat Soc Ser B Stat Methodol 1982;44(3):406–13.
[40] Smith TE. Comparative analysis of point pattern points. Technical report, Philadelphia, USA: University of Pennsylvania; 2020.
[41] Bivand RS, Pebesma E, Gómez-Rubio V. Applied spatial data analysis with R. New York: Springer; 2013, p. 173–211.
[42] Baddeley A, Rubak E, Turner R. Spatial point patterns- Methodology and applications with R. Chapman & hall interdisciplinary statistics series, CRC Press; 2016.
[43] Hansen BE. Lecture notes on nonparametrics. Technical report, University of Wisconsin; 2009.
[44] Diggle PJ. A kernel method for smoothing point process data. J R Stat Soc Ser C (Appl Stat) 1985;34(2):138–47.
[45] Loader C. Local regression and likelihood. Springer; 1999.
[46] Cronie O, Van Lieshout MNM. A non-model-based approach to bandwidth selection for kernel estimators of spatial intensity functions. Biometrika 2018;105(2):455–62.
[47] Diggle PJ. Statistical analysis of spatial and spatio-temporal point patterns. Chapman & Hall/CRC monographs on statistics & applied probability, CRC Press; 2013.
[48] Scott DW. Multivariate density estimation: Theory, practice and visualization. wiley; 1992.
[49] Amaya-Gómez R, Bastidas-Arteaga E, Schoefs F, Muñoz F, Sánchez-Silva M. A condition-based dynamic segmentation of large systems using a Changepoints algorithm: A corroding pipeline case. Struct Saf 2020;84:101912.
[50] Pandey MD, Lu D. Estimation of parameters of degradation growth rate distribution from noisy measurement data. Struct Saf 2013;43:60–9.
[51] Weldon DG. Failure analysis of paints and coatings. Wiley; 2009.
[52] Lee SH, Oh WK, Kim JG. Acceleration and quantitative evaluation of degradation for corrosion protective coatings on buried pipeline: Part II. Application to the evaluation of polyethylene and coal-tar enamel coatings. Prog Org Coat 2013;76(4):784–9.
[53] Melchers RE. A review of trends for corrosion loss and pit depth in longer-term exposures. Corros Mater Degradat 2020;1(1):42–58.
[54] Turnbull A. Corrosion pitting and environmentally assisted small crack growth. Proc R Soc A Math Phys Eng Sci 2014;470(2169):20140254.
[55] Fabas A, Monceau D, Doublet S, Rouaix-Vande A. Modelling of the kinetics of pitting corrosion by metal dusting. Corros Sci 2015;98:592–604.
[56] Valor A, Alfonso L, Caleyo F, Vidal J, Perez-Baruch E, Hallen JM. The negative binomial distribution as a model for external corrosion defect counts in buried pipelines. Corros Sci 2015;101(Supplement C):114–31.